

1 Nuclear Fusion (FUSION): Plasma Heating Systems – Microwave Plasma Heating & Current Drive Systems –

1.1 Microwave Heating System for W7-X (PMW)

Electron cyclotron resonance heating (ECRH) and current drive (ECCD) are the standard methods for localized heating and current drive in future fusion experiments and the only CW heating methods available today. Thus, ECRH will be the basic day-one heating system for the stellarator W7-X which started operation end of 2015 at IPP Greifswald. The ECRH system for W7-X and the project PMW were finalized in 2016. In its first stage W7-X will be equipped with a 10 MW ECRH system operating at 140 GHz in continuous wave (CW).

The complete ECRH system is coordinated by the project “Projekt Mikrowellenheizung für W7-X (PMW)”. PMW has been established by KIT together with IPP and several EU partners in 1998. The responsibility of PMW covers the design, development, construction, installation and system tests of all components required for stationary plasma heating on site at IPP Greifswald. PMW coordinates the contribution from Institute of Interfacial Process Engineering and Plasma Technology (IGVP) of the University of Stuttgart too. IGVP is responsible for the microwave transmission system and part of the power supply (HV-system). IPP Greifswald is responsible for the in-vessel components and for the in-house auxiliary systems. PMW benefits from the collaboration with Swiss Plasma Center (SPC, former Centre de Recherche de Physique des Plasmas, CRPP) Lausanne, Commissariat à l’Energie Atomique (CEA), Cadarache and Thales Electron Devices (TED), Vélizy.

Additional to the successfully running two prototypes, seven series gyrotrons have been ordered from the industrial partner Thales Electron Devices (TED), Vélizy. First operation and long pulse conditioning of these gyrotrons is being performed at the teststand at KIT. Pulses up to 180 s duration at full power are possible (factory acceptance test, FAT) whereas 30 minutes shots at full power are possible at IPP (necessary for site acceptance test, SAT). Including the pre-prototype tube, the prototype tube and a 140 GHz CPI tube, in total 10 gyrotrons will be available for W7-X. To operate these gyrotrons eight superconducting magnet systems have been manufactured at Cryomagnetics Inc., Oak Ridge, USA and in addition one system at Oxford Instruments and Accel.

In 2016 the Site Acceptance Tests of the TED series gyrotron SN5i could be finished successfully at IPP Greifswald. Stable operation of the tube at RF power of 900 kW has been shown and quasi steady state operation (1440 s) at full power has been demonstrated. Since 2016 there are 8 TED Gyrotrons operable on site at IPP Greifswald with a total RF power above 7000 kW.

Due to successful operation, IPP ordered an additional series gyrotron (SN8). Delivery and installation is expected for 2017.

The ECRH system has been used as regular plasma start-up and heating system for the first Hydrogene experimental campaign of W7-X. With the ECRH system up to 6 MW RF power has been injected into the plasma, reliable plasma operation has been achieved up to 6 s.

1.2 Experimental Verification of the EU 170GHz, 1MW industrial prototype gyrotron for ITER

1.2.1 Introduction

The European Gyrotron Consortium (EGYC), in cooperation with its industrial partner Thales Electron Devices (TED), has designed and developed the EU 1 MW - 170 GHz gyrotron for ECH&CD on ITER, under the coordination of the European domestic agency F4E. According to the project strategy followed by F4E, two prototypes were developed. The first one is a modular short-pulse (SP) prototype tube built for validating the design, in terms of generated RF power, efficiency and quality of the RF output beam of the main gyrotron components for millisecond pulses. The second prototype is a long-pulse industrial tube with the additional goal to fulfill the ITER requirements in terms of pulse length and continuous wave (CW) operation regime. The technological design of the gyrotron was decided to resemble as much as possible the 1 MW, 140 GHz CW Wendelstein W7-X gyrotron in order to take advantage of the experience gained during the manufacturing of the 7 tubes of the industrial series production (+2 prototypes). The CW tube was delivered to KIT and prepared for the operation at the beginning of 2016. The first experiments with the goal to optimize the operation of the CW prototype in the short-pulse regime started in February 2016. In June 2016 preparation for the CW operation of the tube started with the goal to extend the pulse duration up to 3 minutes. The tests with the 1MW CW prototype will be continued at longer pulse lengths in the European Gyrotron Test Stand at EPFL-SPC in Lausanne.

1.2.2 Delivery and installation

The 1MW, CW gyrotron prototype has been delivered at KIT on January 18, 2016 together with all the necessary auxiliaries, such as the collector water jacket, the longitudinal and transversal sweeping coils and ion-getter pump power supplies (Fig. 1.2.1). After delivery the shock sensors have been examined thoroughly and it was confirmed that there were no incidents during the transportation from Velizy to Karlsruhe. In order to check the internal pressure of the tube, a power supply has been connected to one of the Ion-Getter-Pumps of the gyrotron and the measured current was found smaller than 10^{-7} A ($< 10^{-9}$ mbar), confirming the excellent vacuum conditions of the tube. Fig. 1.2.2 shows the gyrotron after installation in the cryostat and connection of all auxiliaries and cooling systems.



Fig. 1.2.1: Delivery and unpacking of the gyrotron



Fig. 1.2.2: First industrial ITER gyrotron after final installation at KIT in the OI Magnet.

1.2.3 Preparation for the experiments

Magnetic field alignment

Before the gyrotron was installed in the magnet, a verification of the alignment magnetic field axis of the magnet, was performed by using the measurement equipment available at KIT. The device consists of a system of hall-probes that deliver the information of the magnetic field components in longitudinal and radial direction. By moving of the probe along the mechanical axis of the magnet and additional azimuthal rotation the data were collected. Based on further computation of the data a position of the magnetic field axis with respect to the mechanical axis of the magnet was defined. The performed tests confirmed a perfect alignment of the magnet. The maximal displacement of the magnetic and mechanical axis was below 0.1 mm in the whole analyzed region, which is below the mechanical accuracy of the measurement system. The tilt of the magnetic field axis was estimated to be close to 0.14 mrad.

Preparation of the oil tank

One of the most critical regions of the gyrotron setup is the oil tank, where HV connections, cooling pipes and electric supply cables for the electron gun and NC-coil exist in very limited space. The following connections have been established before the start of the tests inside the oil tank (Fig. 1.2.3):

- 1) Cathode voltage
- 2) Filament heating
- 3) Cooling of the emitter cathode
- 4) Depression "body" voltage (using "wire" connection)
- 5) Cooling of the NC-coil
- 6) Electric supply cables for NC-coil

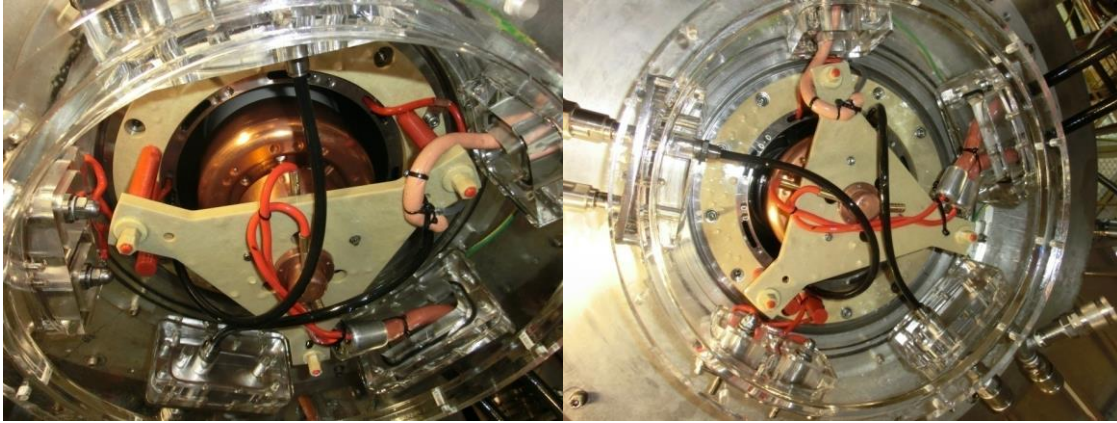


Fig. 1.2.3: Oil tank after installation of HV, electrical connections and cooling pipes.

Voltage Stand-off

The voltage stand-off properties of the gyrotron were tested with the gyrotron installed in the cryostat and with all auxiliaries prepared for CW operation. The measurements were repeated both with the magnetic field activated and deactivated. It is worthwhile to mention that before continuing to CW operation of the tube, the isolating oil that was used during the SP phase of the experimental campaign and after the stand-off measurement was replaced by fresh oil of the same type and quality in order to ensure that the isolation quality was the maximum possible.

The HV properties of the cathode to ground were measured with the gyrotron installed in the cryostat and prepared for CW operation. For such a measurement the cathode and the filament are short circuited between each other and connected to the negative pole of the high-impedance power supply, whereas the body is connected to the ground. Fig. 1.2.4 summarizes the measurements of this configuration using the typical Fowler-Nordheim curves. In detail, the red curve corresponds to measurements with the magnetic field activated and the black curve in the absence of magnetic field. In the same figure the green line presents the corresponding measurements performed by TED at Velizy during the FAT test and before the delivery of the tube at KIT. It was possible to increase the voltage up to 96 kV without any particular reaction of the tube. This value is much higher from the highest voltage that would be needed for operation of the gyrotron at the HVOP, namely 80 kV. For this reason no further attempt to increase the voltage was performed.

Similar measurements were performed with the cathode and filament short-circuited between each other and connected to ground, while the body was connected to the positive pole of a current limiting high-voltage power supply. The measurement taken are summarized in Fig. 1.2.5, the black line corresponds to the voltage stand-off properties that were measured during the FAT test, The red and green curves corresponds to measurements without and with the magnetic field activated, respectively, yet without water flow in the cooling circuit. Finally the blue and orange curves correspond to the case where water is flowing in the cooling system. In this configuration it is possible, both in the presence and the absence of the magnetic field, to increase the voltage of the body up to 32 kV without arcing incidents or changes in the quality of the vacuum.

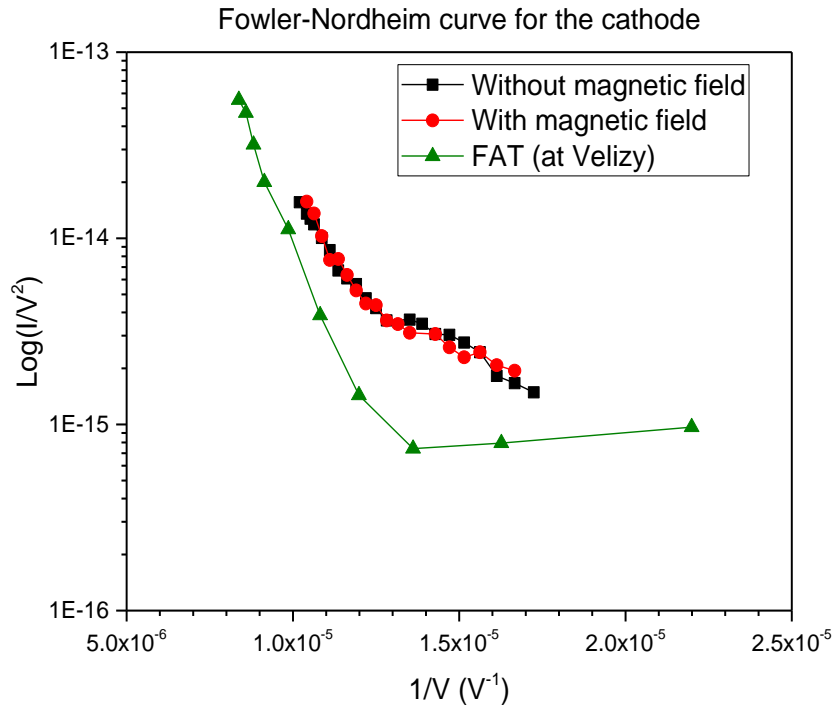


Fig. 1.2.4: Fowler-Nordheim diagram with the cathode on high voltage and the body grounded (maximum voltage applied 96 kV).

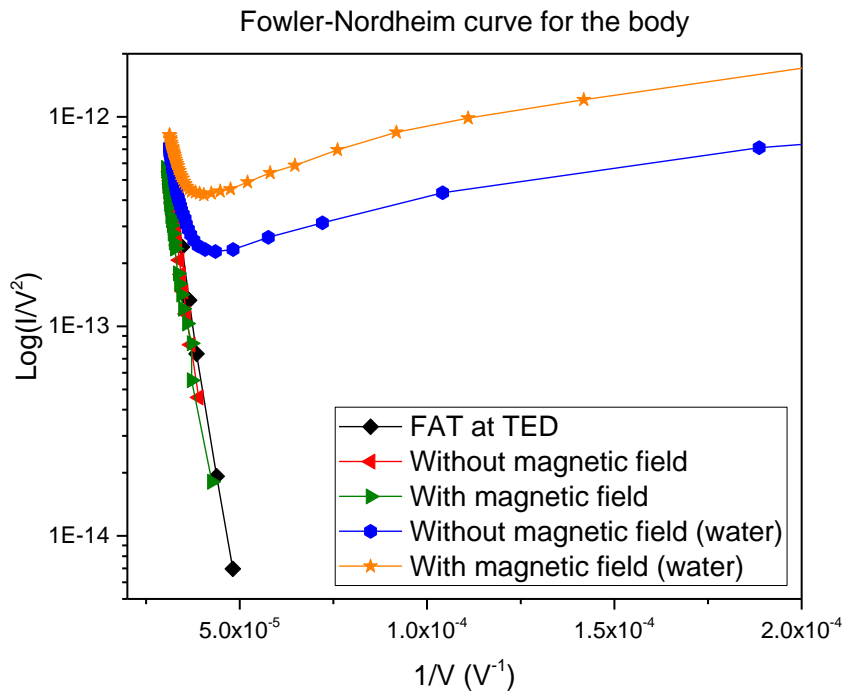


Fig. 1.2.5: Fowler-Nordheim diagram with the body on high voltage and the cathode grounded (maximum voltage applied 32 kV).

Verification of the filament heater

The test of the filament heater was performed by investigating the dependence of the voltage on the applied current. The achieved V/I -profile has been plotted and compared with similar measurements from other gyrotrons (i.e. from W7-X project), equipped with similar type of filament heater. The comparison of the measured data (SAT) are presented in Fig. 1.2.6.

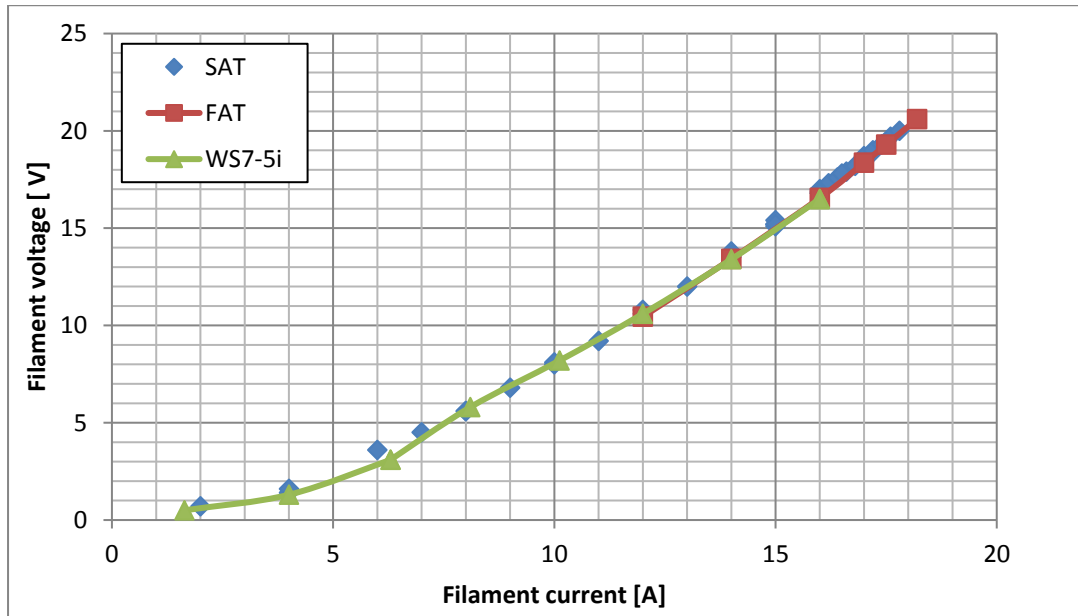


Fig. 1.2.6: Filament current vs. filament voltage (SAT) as comparison with the FAT and W7-X SN5i gyrotron results.

Electron gun emission uniformity investigation

In order to characterize the emission uniformity of the gun, the emitted current with respect to the accelerating voltage (V/I curves) was measured (Fig. 1.2.7). Based on that data, a study of the transient region between the space charge limited and temperature limited regions was performed, giving feedback about the distribution of the electron emission from the cathode. V/I curves were measured for different temperatures (filament heating current values) of the emitter ring. For each of them the standard deviation of the normalized current density distribution δJ was calculated. This factor is a measure of the emission uniformity and a small value corresponds to good uniformity in emission density. In this case it has been calculated to be around 0.24. Although it is not very small, it is an acceptable value.

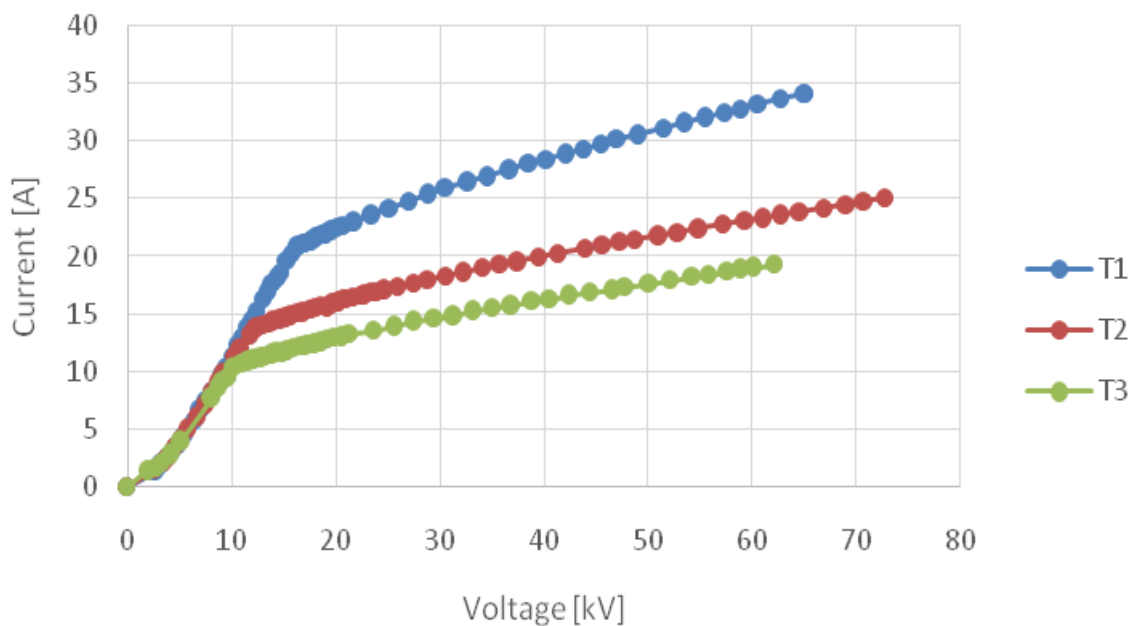


Fig. 1.2.7: Emitted current vs. accelerating voltage for three different temperatures of the emitter ($T_1 > T_2 > T_3$).

1.2.4 Short-Pulse (SP) Operation

Experimental Setup

In order to get an overview of the performance of the tube and to compare the experimental results achieved with the SP prototype tube, the CW version was at first operated in the short pulse regime (pulse length <10 ms). The gyrotron was equipped with power diagnostic systems such as a low power flow calorimeter and a bolometer. The flow calorimeter delivered information about the actual RF output power transmitted through the window and the bolometer information regarding the internal stray radiation. In addition, the gyrotron was connected to the frequency measurement system (filter bank and frequency time analyzer (FTA), and/or PSA-system). The frequency measurement systems delivered information about the output frequency of the main mode, mode competition in the cavity and parasitic modes excitation inside the tube.

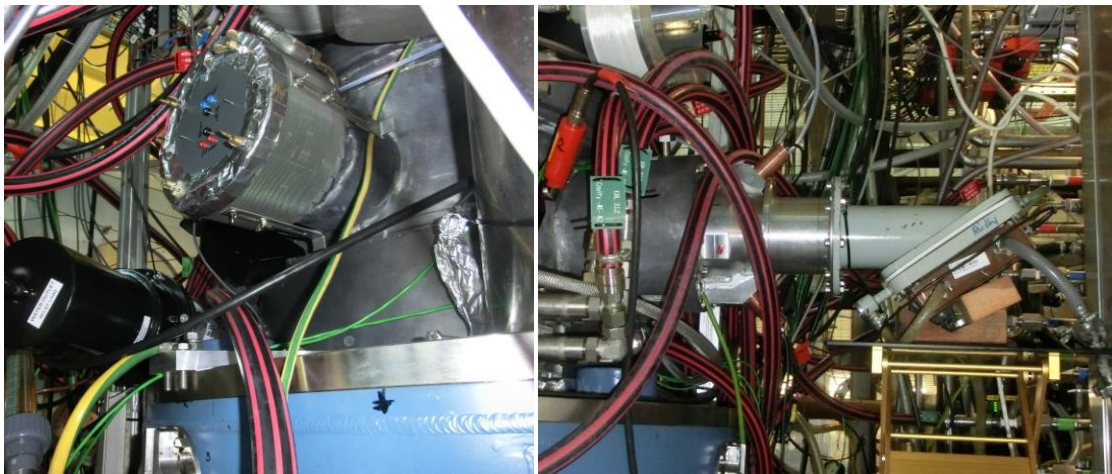


Fig. 1.2.8: Bolometer (stray radiation level monitoring) (left) and flow-calorimeter (measurement of the output power) (right).

Gyrotron Alignment

The verification of the alignment of the magnetic field with respect to the axis of the gyrotron cavity has been performed using a method developed at KIT and used with several other high-power gyrotrons. It is based on the symmetry study of the excitation region of the main mode. The idea is to introduce a radial displacement of the electron beam at the cavity by energizing a set of dipole coils and monitor the influence of this displacement on the excitation of a cavity mode. During the displacement of the electron beam using the dipole coils, a switching point between the main mode and its neighboring competitors is recorded and presented graphically. In the optimal case a circle is formed, which surrounds the dipole currents region, where the main mode is being excited. The displacement of the center of the mode excitation circle from the origin of the dipole coils coordinate system (zero current in both directions) provides an indication regarding the misalignment of the magnetic field to the gyrotron cavity axis. For the industrial prototype, the center of the mode excitation circle of the main mode $TE_{32,9}$ was estimated to be at $I_x/I_y=15\text{ A}/11\text{ A}$ ($I_{x,y} = 1\text{ A}$ corresponds to a shift of 0.037 mm according simulation). In order to align properly the beam in the cavity dipole coils current +15A/+11A were used. Note, that the compensation of the electron beam position take place only in the cavity region, the position of the magnetic field at the gun region is not affected by that.

Operational Maps

Setting properly the three independent currents of the OI magnet it is possible to have the appropriate magnetic field intensity at the cavity for different combinations of the angle of the magnetic field lines on the surface of the emitter and the beam radius R_b in the cavity region. Note that the magnetic field angle in the emitter region φ_b , with respect to the gyrotron axis, is a significant operating parameter related to the average pitch factor of the electron beam. Fig. 1.2.9 represents the operational map of the gyrotron i.e. the RF power generated (Fig. 1.2.9a) and the achieved efficiency (Fig. 1.2.9b) with respect to the magnetic field angle and the beam radius in the cavity. For each operating point the maximal possible accelerating voltage has been applied before switching to the neighboring mode. The corresponding simulated values of the average pitch factor of the electron beam are presented in Fig. 1.2.9c. The measurements for the operational map have been performed after proper alignment of the electron beam in the cavity using the dipole coils of the OI superconducting magnet. Based on the operational maps, the optimal operation points in terms of power and efficiency have been defined. The most interesting operation region was discovered at $\varphi_b = -2^\circ$ and $R_b = 9.55$ mm. As an alternative, the operating point at $\varphi_b = -1^\circ$ and $R_b = 9.45$ mm can also be taken into account.

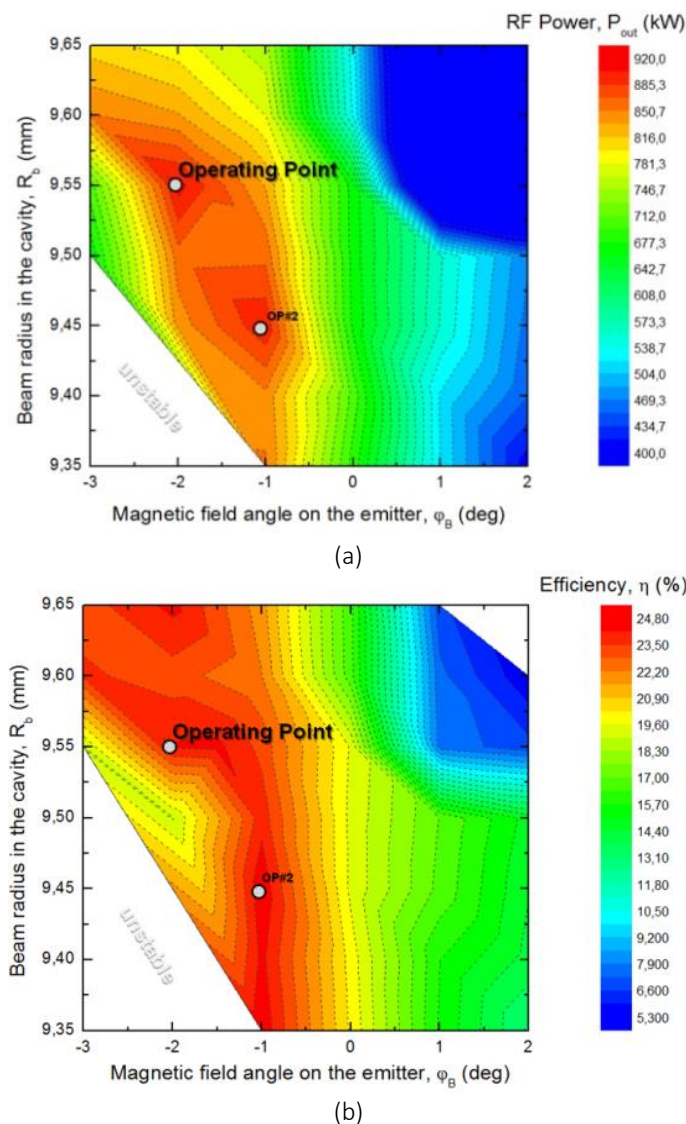


Fig. 1.2.9: (a) Generated RF power and (b) Efficiency with the magnetic field angle φ_b and the beam radius R_b in the cavity.

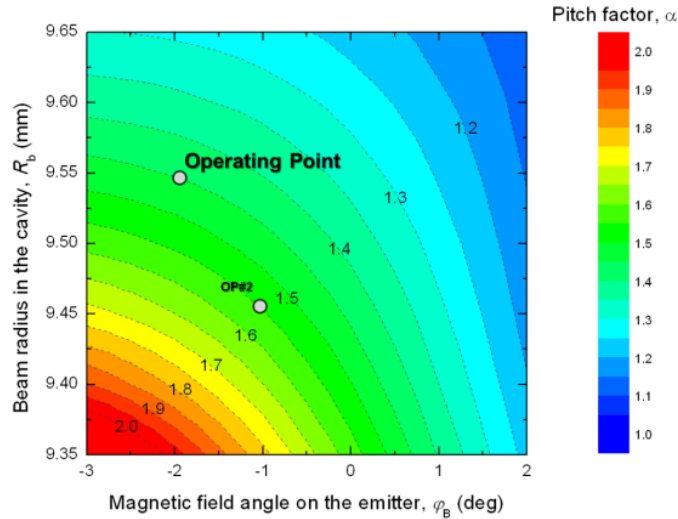


Fig. 1.2.10: Simulated Electron beam pitch factor

RF Power with respect to acceleration voltage

Due to the very stable performance of the gyrotron, the Low-Voltage Operating Point (LVOP) has been selected for the first experiments in non-depressed collector operation. Based on the above described optimal operating point the gyrotron was operated with electron beam radius $R_b = 9.55 \text{ mm}$ and magnetic field angle at the emitter $\varphi_b = -2^\circ$, using dipole coils currents $I_x = 15 \text{ A}$ and $I_y = 11 \text{ A}$. Operation with beam current $I_b = 48 \text{ A}$ and accelerating voltage 76.8 kV gave RF power $\sim 930 \text{ kW}$ with efficiency $\sim 25 \%$. By increasing the electron beam current higher than the nominal parameters ($I_b = 53 \text{ A}$ and $V_a = 78 \text{ kV}$) and after adjustment of the dipole coils ($I_x/I_y=20 \text{ A}/13 \text{ A}$), it was possible to obtain 980 kW .

The dependency of the power and the efficiency on the accelerating voltage are presented in Fig. 1.2.11. The resulted RF power has been compared with theoretical calculations from the in-house EURIDICE code, and were found in agreement as presented in Fig. 1.2.12. The measured and theoretically expected dependency of the output frequency on the accelerating voltage is presented in Fig. 1.2.13. Taking into account the accuracy of cavity fabrication ($20 \mu\text{m}$), which corresponds to $\sim 200 \text{ MHz}$ frequency shift, very good agreement has been achieved between theory and experiment.

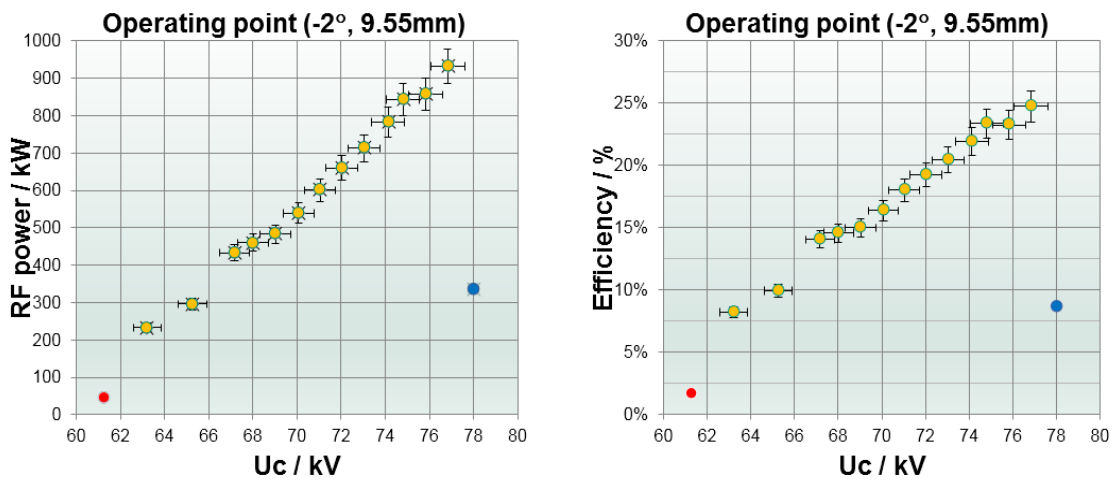


Fig. 1.2.11: RF generated power and efficiency vs. accelerating voltage achieved at LVOP with the beam current $\sim 48 \text{ A}$.

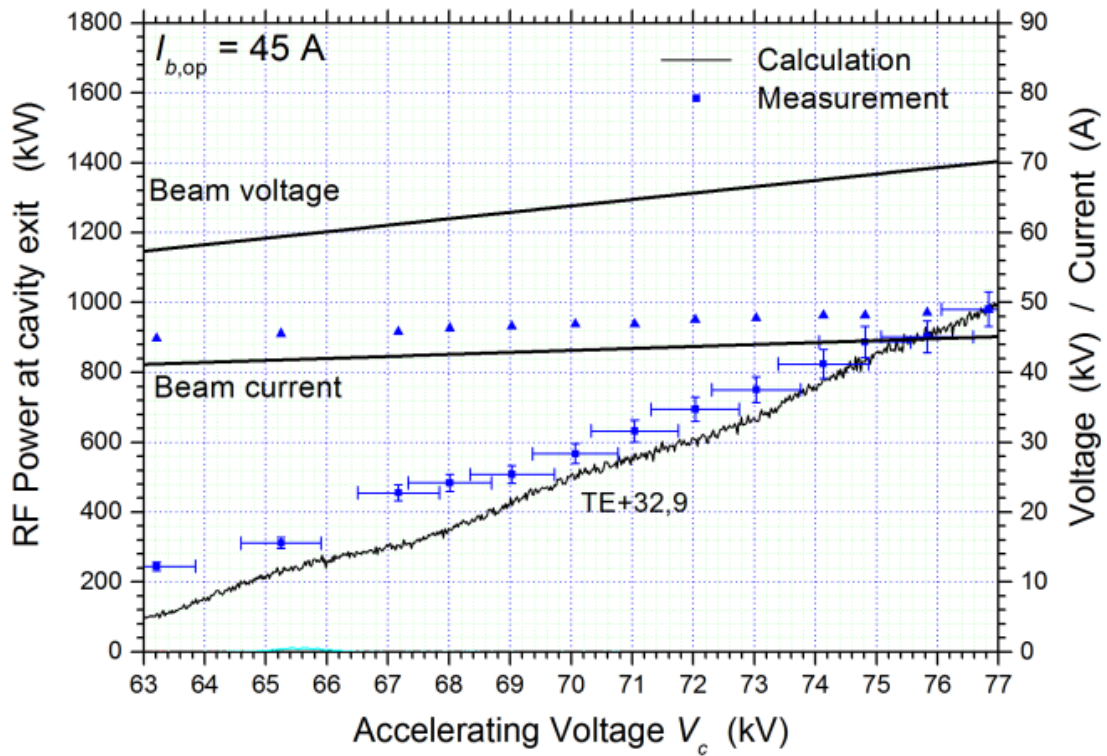


Fig. 1.2.12: Generated power vs. the beam voltage and comparison with simulated results from the code suite EURIDICE.

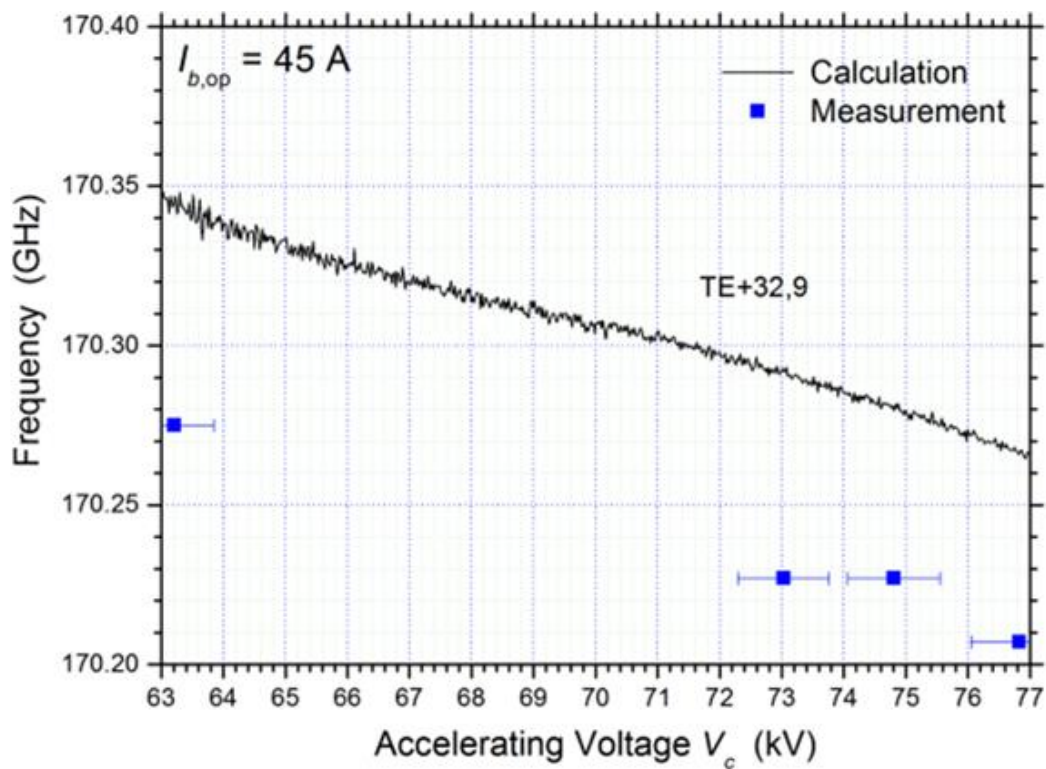


Fig. 1.2.13: Dependency of the gyrotron output frequency on accelerating voltage.

Parasitic oscillations

There are three diagnostic systems which are available for the assessment of the parasitic oscillations activity in the tube. In detail, a bolometer is installed in front of the relief window of the tube in order to assess the level of the stray radiation in the tube. In addition a waveguide is installed either on the side of the relief window or on the diamond window and transmits signal to a nine 2 GHz channel filter-bank, as well as to the more sophisticated PSA frequency measurement system. Depending on the actual value of the accelerating voltage and the beam current, it was possible in some cases to identify parasitic signals with frequencies approximately 20 GHz lower than the frequency of the operating mode. However, these signals did not seem to limit the operation of the tube.

RF Beam Profile Measurements

The first preliminary verification of the position and shape of the RF beam is usually performed using a simple thermal paper placed at the output window. The gyrotron operates in the short pulse regime (<1 ms) and delivers enough energy to create a burn spot on the thermal paper which corresponds to the real shape of the RF beam and indicates the position of the microwave at the window. Based on that procedure first verification of the efficiency of the mode converter and adjustment of its q.o subcomponents (launcher, mirrors) can be done. The information about the position of the RF beam at the output window is extremely important for the continuation of the experimental campaign and further conditioning procedure of the tube, before the more accurately investigation on the Gaussian mode content with the IR camera is taking place. The preliminary result of the measurement with thermo-paper are presented in the Fig. 1.2.14. They confirmed that the RF beam seems to be well aligned to the window center with the estimated shift to be approximately 5 mm to 5 o'clock position.

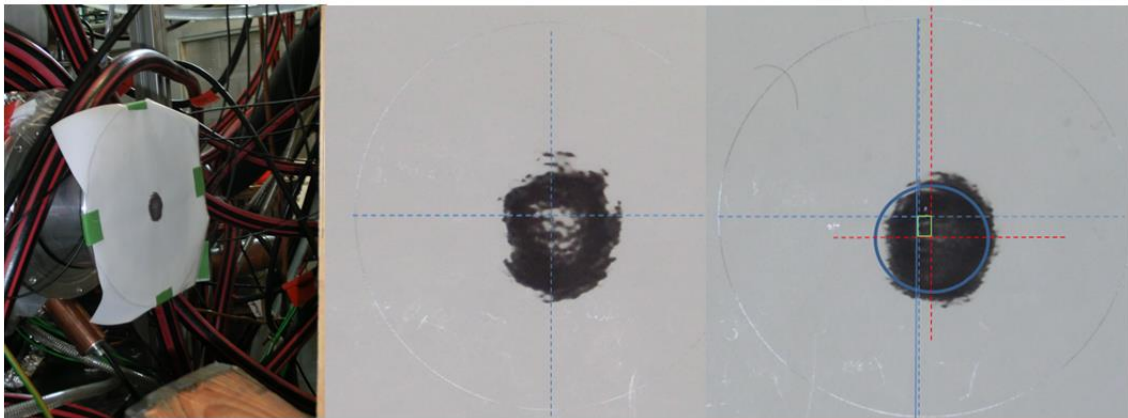


Fig. 1.2.14: Preliminary results of the beam profile measurements at the output window achieved with thermal paper.

The thermal footprint of the gyrotron RF beam has been imaged on 200 mm diameter target plates, made either from PVC (with the thickness adjusted for 170 GHz, in order to avoid any reflections) or regular office printer paper. The targets were positioned along the RF beam path at distances between 180 and 1300 mm (in 100 mm increments) from the gyrotron output window using a motorized movement stage. It is extremely important to have several measurements inside the Rayleigh range and near to the beam waist position otherwise the phase reconstruction method will fail. The targets were perpendicular to the nominal beam axis of the gyrotron, with a 3° horizontal tilt to avoid direct reflection of the beam into the gyrotron. The IR camera was looking at the target from behind, with the camera offset horizontally from the beam axis by about 300 mm. The beam dump behind the target was a 50 mm thick PVC plate angled horizontally to be fully absorbing and to avoid any reflection. The arrangement of the measurements setup is presented in Fig. 1.2.15. Pulse lengths between 0.3 ms and 3 ms were used in order to achieve an optimal

temperature and measurement dynamic depending on the size of the RF beam spot on the target (Fig. 1.2.15) and its distance from the output window. According to the post processing of the measurements, the Gaussian content of the beam is found to be 97%. The most important beam parameters are summarized in Table 1.2.1.

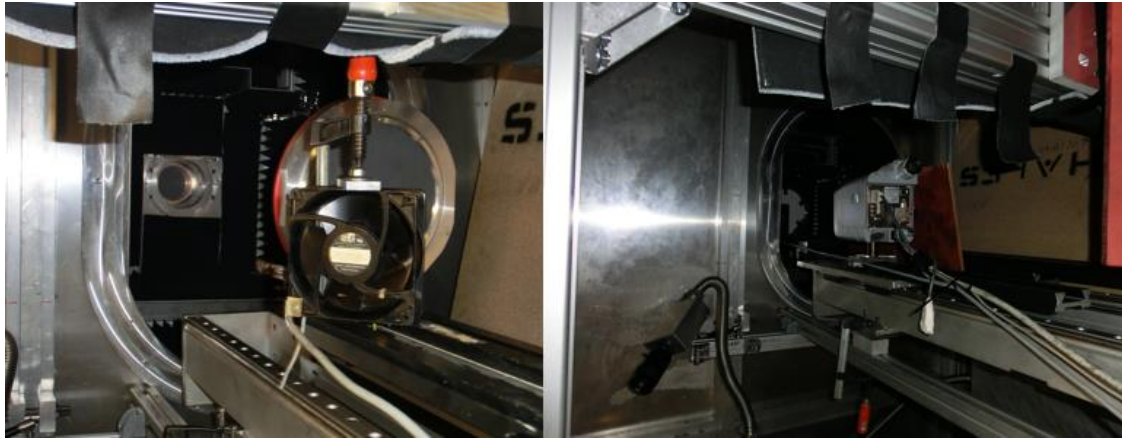


Fig. 1.2.15: Arrangement of the IR beam profile measurement setup.

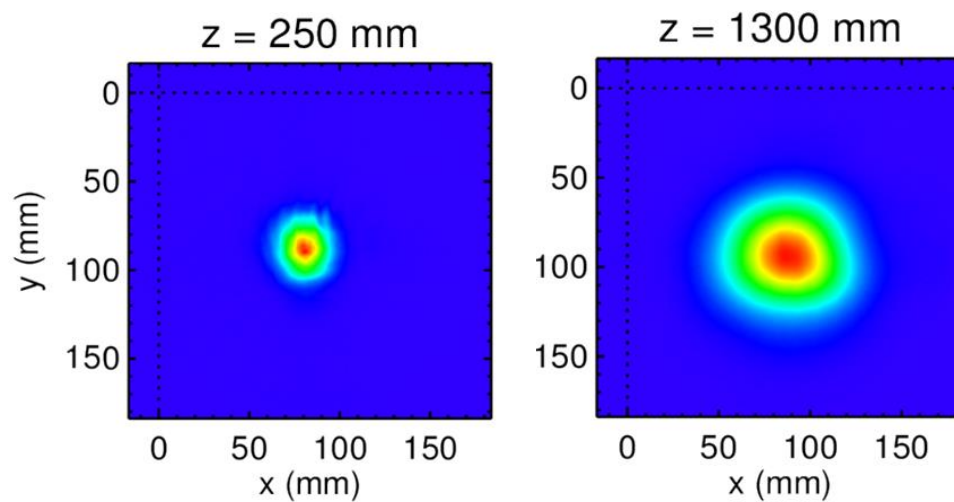


Fig. 1.2.16. Thermographic images from the microwave output beam of the gyrotron recorded on a PVC-target at different distances z from the gyrotron window.

Table 1.2.1: RF beam properties

Parameter	X direction	Y direction
Gaussian content	0.97	
Beam waist (mm)	18.3	21.5
Waist position (mm)	28	28
Beam tilt (mm/m)	7.8	6.0
Beam shift at the window plane (mm)	-4.9	2.7

1.2.5 Long Pulse (CW) Operation

Microwave Box and Diagnostics

Fig. 1.2.17 depicts the main quasi-optical components and diagnostics installed inside the microwave box of the KIT test-stand. The RF beam that exits the diamond window of the gyrotron is driven to the load entrance by subsequent reflections on four mirrors. The position of the mirrors is carefully adjusted by recording the footprint of the beam on thermal paper in order to have the beam well aligned around their center. Fig. 1.2.18 presents the footprint of the RF beam on thermal paper placed at the back side of the microwave load, at the position where a conical mirror is placed in order to scatter and distribute the microwave power along the surface of the load by subsequent reflections on the load wall.

Special care is given also on the angle of mirror 1 with respect to the RF beam line, since this control the coupling factor of the waveguide coupler that is realized on the surface of the mirror 1 and in turn the amplitude of the signal that is guided by a short waveguide to a RF diode that is used to detect mode loss and deactivate the gyrotron to avoid possibility of damage due to excitation of a wrong mode (mode loss interlock). An additional signal taken from the relief window is also transmitted with a waveguide to the frequency measurement related systems, namely the filter-bank, frequency measurement and the PSA system. The signal from the relief window is preferred for such measurements, since the extraction efficiency of parasitic signals is low from the diamond window, especially in a distance similar to the one between the diamond window and mirror 1.

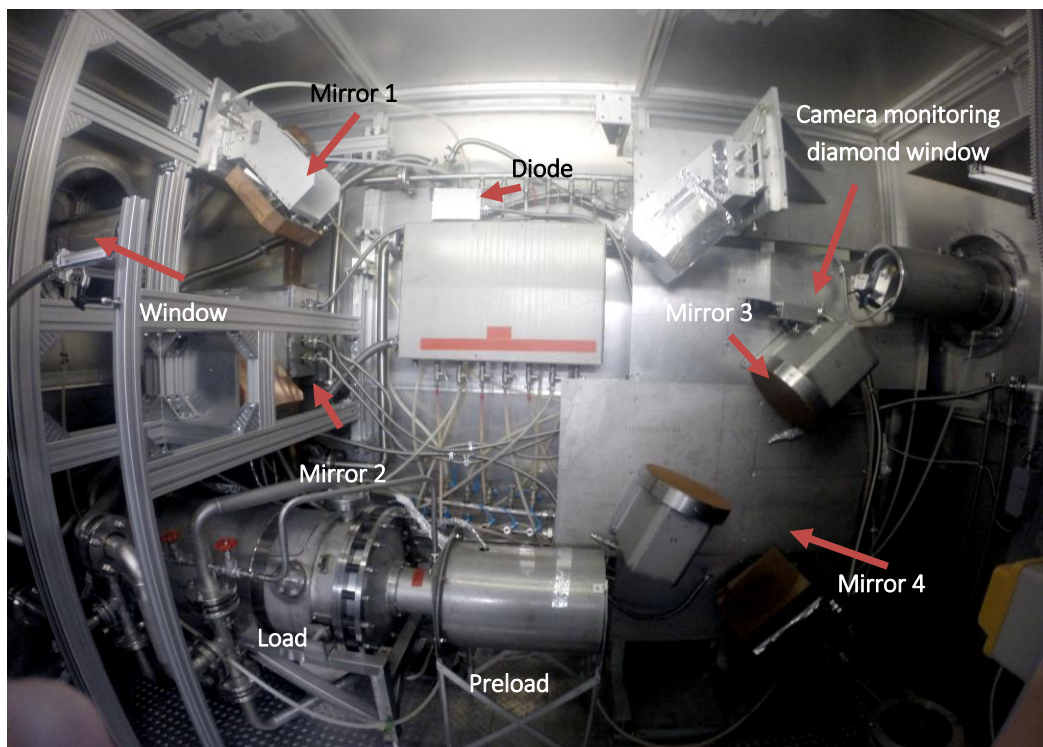


Fig. 1.2.17: Microwave box prepared for CW operation of the gyrotron.



Fig. 1.2.18: Thermal paper shot at the back side of the microwave load (at the position where the conical mirror is mounted).

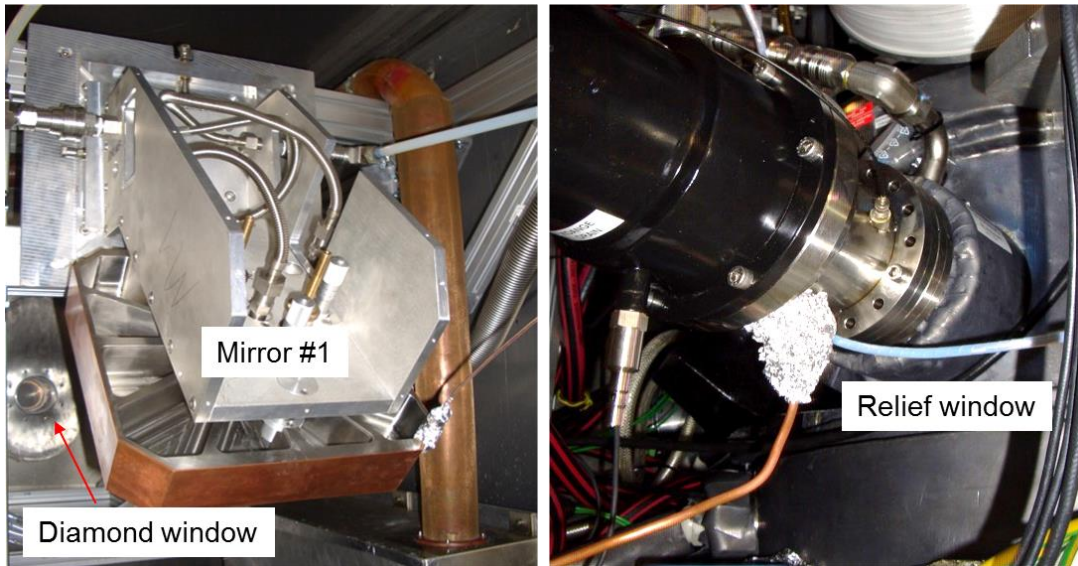


Fig. 1.2.19: Diagnostics installed inside the microwave box and at the relief window.

Performance in CW

After the conditioning of the collector the operational parameters were progressively increased to excite RF oscillations with the goal to elongate the pulse duration from the millisecond regime to the three minutes regime. Fig. 1.2.20 represents the length of some representative pulses (in terms of length and output power) that were achieved during several days of the CW experimental campaign with respect to the date. The RF conditioning started a few weeks earlier (approximately on 15/9/2016), increasing the necessary time to proceed from short pulse to long pulse regime to approximately seven weeks.

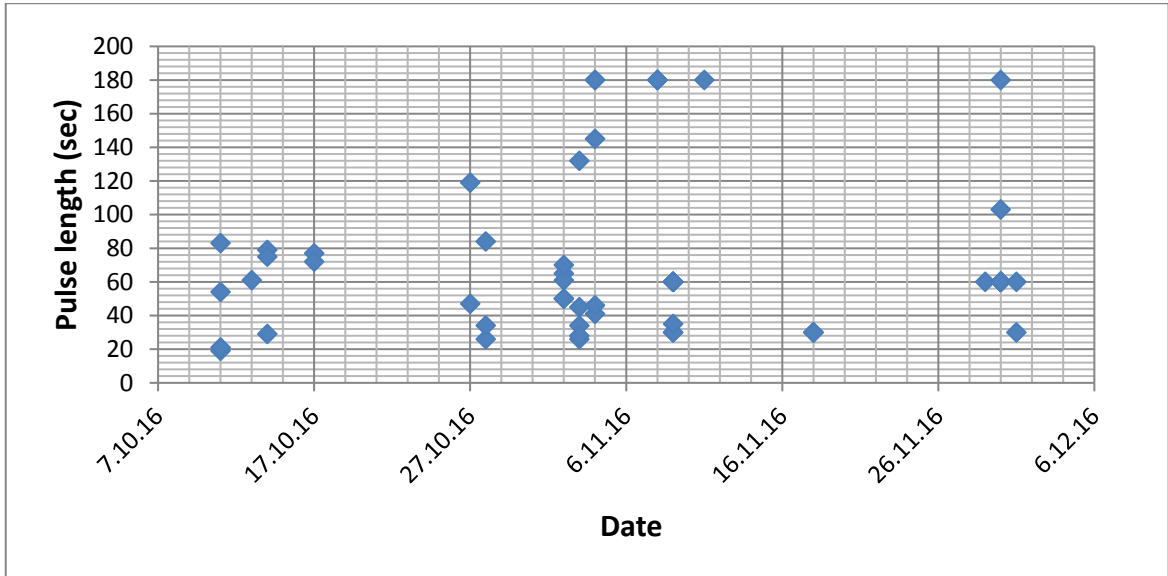


Fig. 1.2.20: Evolution of the pulse length achieved during the conditioning of the tube with RF.

Fig. 1.2.21 presents the operational parameters of a three minutes pulse that was achieved with the industrial prototype. During this pulse the average generated power was 786 kW with accelerating voltage 72.2 kV (including 24.6 kV of depression voltage) and beam current 44.4 A, getting in this way an overall efficiency of 37.2 %. During the pulse the vacuum level was less than 1 μ A, whereas a few visible peaks are a result of conditioning events. Considering that at the moment the tube is sufficiently conditioned with RF a vacuum level in the range 0.6-0.8 V (Midivac power supply) should be expected, which corresponds to less than 1 μ A.

Fig. 1.2.22 presents the temperature of all the collector thermocouples with respect to the time during the same pulse. The maximum temperature of the collector at the end of the pulse reaches almost 190 °C mainly due to the low depression voltage that is used.

Fig. 1.2.23 presents the typical light distribution that is observed on the surface of the diamond window during the operation of the tube with long pulses.



Fig. 1.2.21: 180 sec pulse achieved during the experiments. In the figure it is visible the beam current (blue), the accelerating voltage (black), the cathode voltage (green), the depression voltage (red), the vacuum reaction (yellow) and the mode-loss diode signal (magenta).

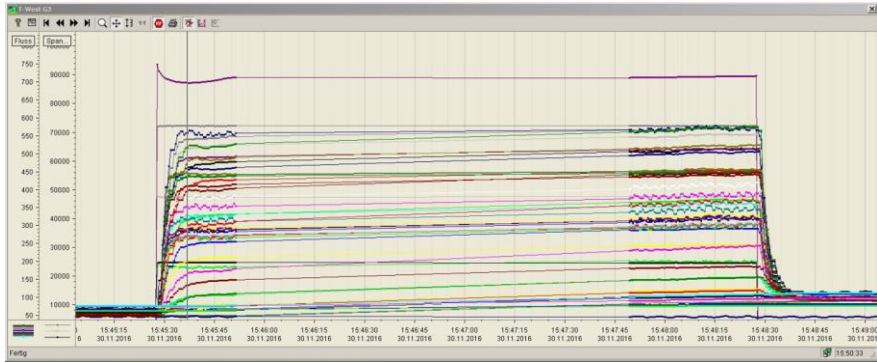


Fig. 1.2.22: Collector's thermocouple temperature and I_{beam} during a 180 sec pulse.

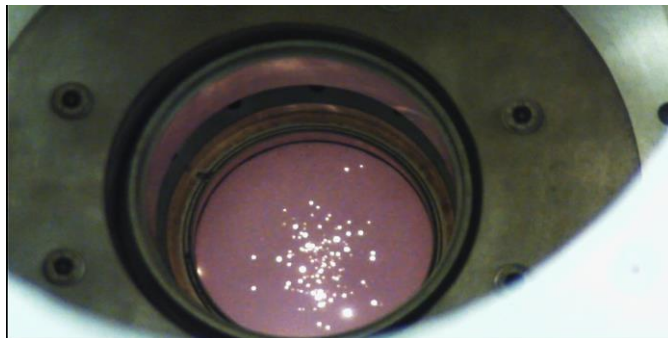


Fig. 1.2.23: "Stars constellation" on the diamond window during CW operation

Calorimetry system

The generated power and the dissipated losses on the internal component of the gyrotron as well as of the auxiliaries in the microwave box are monitored using a calorimetry system. Fig. 1.2.24 presents the power measurements that were recorded for a ~800 kW - 180 s pulse. All measured values expressed as a percentage of the input and the generated power are summarized in Table 1.2.2. It is interesting to note that in most cases the calorimetrically measured power approaches 99 % of the electrical input beam power. In addition the internal losses (internal components of the tube) are in the level of 5 % with respect to the RF power at the diamond window, whereas the external losses (inside the microwave box) are in the range of 2-3 %.

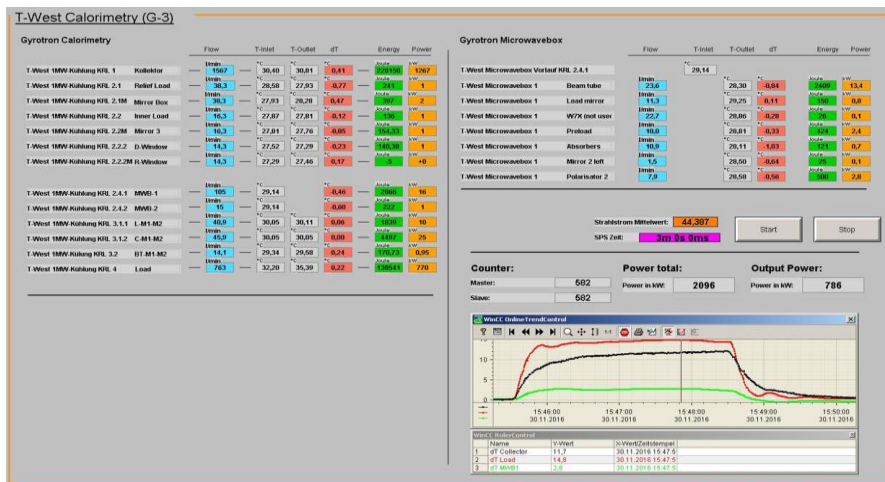


Fig. 1.2.24: Calorimetry measurements during a 180sec pulse.

Table 1.2.2: Power balance for a 180 sec pulse.

ITER CW, 30.11.2016			Power [kW]	Power [%] w.r.t. total generated	Power [%] w.r.t. output power	Power [%] w.r.t. input power
	Ucath (kV)	Ib (A)				
Input power	47.6	44.4	2133.44			
Measurements						
Window			1	0.1	0.1	0.0
Mirror 3			1	0.1	0.1	0.0
Cavity M1-M2			25	3.0	3.2	1.2
Beam tunnel M1-M2			0.95	2.3	0.1	0.0
Mirror Box			2	0.2	0.3	0.1
Launcher M1-M2			10	1.2	1.3	0.5
Kollektor			1267	153.0	161.0	59.9
Inner Load			1	0.1	0.1	0.0
Relief Load			1	0.1	0.1	0.0
Relief Window			0	0.0	0.0	0.0
Water Load			770	93.0	97.8	36.4
Messbox 1			16	1.9	2.0	0.8
Messbox 2			1	0.1	0.1	0.0
Output power			787			99.2
Total generated power			828			
Internal RF losses			41	5.2	5.0	1.9
External RF losses			17	2.2	2.1	

Power and Efficiency

Fig. 1.2.25 presents with colored squares the achieved RF power in long pulse operation with respect to the beam radius at the cavity and with the orientation of the magnetic field lines in the emitter region as a parameter. In the same figure the colored circles represent the corresponding overall efficiency in depressed operation. Although the experimental measurements are quite sparse, there is a visible tendency for increased power and efficiency towards lower beam radii at the cavity and more negative

angles of the magnetic field in the emitter region. The maximum achieved power in 180 s pulses is 786 kW with 37.2 % total efficiency. In detail the cathode voltage was 47.6 kV, the body voltage 24.6 kV and the average beam current 44.4 A.

It is important to mention that the reported power values were obtained for the different operating points using different values of the accelerating voltage and of the beam current. In addition, at each operating point the accelerating voltage is, usually, slightly lower than the maximum possible one, in order to minimize the risk of a mode jump during the cooling phase of the cathode, where the beam current decreases ~ 2 A, depending also on the current boosting scheme that is employed. In addition, the dipole coil currents that are used to better align the electron beam in the cavity, were not further optimized during the long pulse operation of the tube. The values used during power optimization in short pulse were applied. Summarizing, it would be quite possible to further optimize the tube in CW operation in order both to produce slightly more power, as well as to increase the total efficiency of the gyrotron.

Fig. 1.2.26 presents the generated power and the corresponding achieved total efficiency with respect to the depression voltage for the operating point ($-3^\circ/9.50$ mm). The generated power is almost constant with the increase of the depression voltage, which results in an increase of the total efficiency. Depression voltage values higher than 26 kV resulted in body current in the range of 50 mA and instabilities during the first seconds of the pulses, including arcing and current fluctuations.

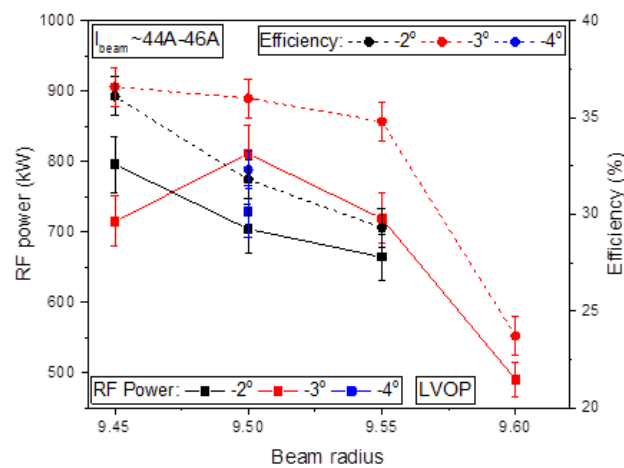


Fig. 1.2.25: RF Power and corresponding overall efficiency with respect to the beam radius and with the orientation of the magnetic field lines at the emitter as a parameter. Operation only at the LVOP.

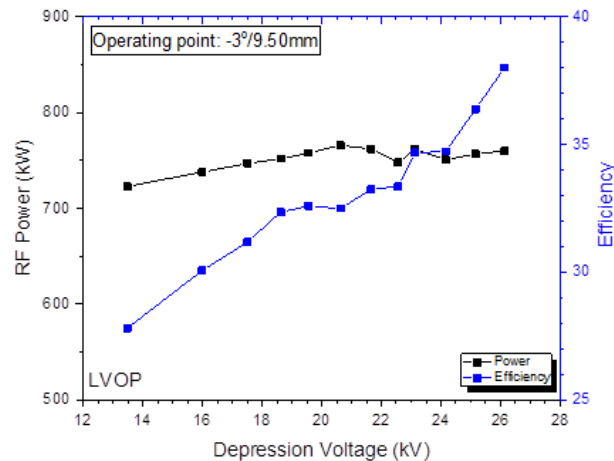


Fig. 1.2.26: RF power and corresponding overall efficiency with respect to the depression voltage for the LVOP.

Frequency dependence

The time dependence of the frequency for the nominal mode $TE_{32,9}$ was recorded using the PSA (Pulsed Spectrum Analysis) measurement system that is available at KIT. Since the maximum acquisition length with full sampling resolution is limited to 14 ms, it is not possible to record continuously a single pulse in CW operation of the gyrotron. For this reason, multiple pulses with similar accelerating voltage and beam current properties were made and by controlling the delay time between the trigger signal of the pulse and the PSA system activation, 1 ms measurements were recorded at different points of time of the respective pulse. Taking into account that the relative spread of the accelerating voltage as well as of the beam current of these pulses are both below 0.1 % we consider this approach to give an adequately accurate image of the frequency drop during the first seconds of a single pulse.

Fig. 1.2.27 presents the frequency of the nominal operating mode of the tube with respect to the time for two different cases of the orientation of the magnetic field line in the area of the emitter, namely -2° (red circles) and -3° (black squares). In both cases the oscillation frequency starts approximately from 170.3 GHz and drops progressively towards 169.95 GHz (frequency drop in the range of 350 MHz) meeting very well the ITER specifications.

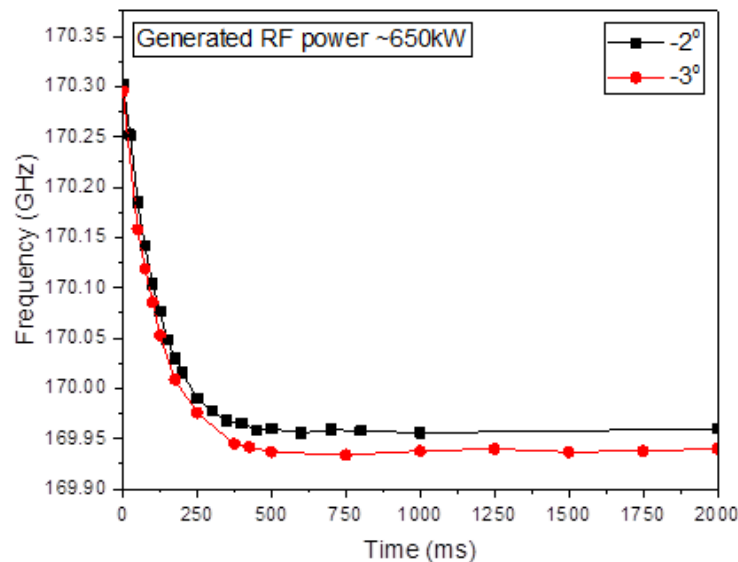


Fig. 1.2.27: Frequency drop with respect to the time.

The above described frequency drop during the pulse is, in general, attributed to the neutralization of the beam during the pulse as well as to the thermal expansion of the cavity, which strongly depends on the generated RF power. In both presented operating points the generated RF power was in the level of ~ 650 kW. The dependence of the frequency drop on the generated power is presented in Fig. 1.2.28, using experimental data from different operating points and making the assumption that the frequency drop is governed by the total generated power and not on the specific operating parameters of the different operating points. Although the data in the 700-800 kW power level are quite scattered, there is approximately 400 MHz frequency drop for 0.8 MW of generated power.

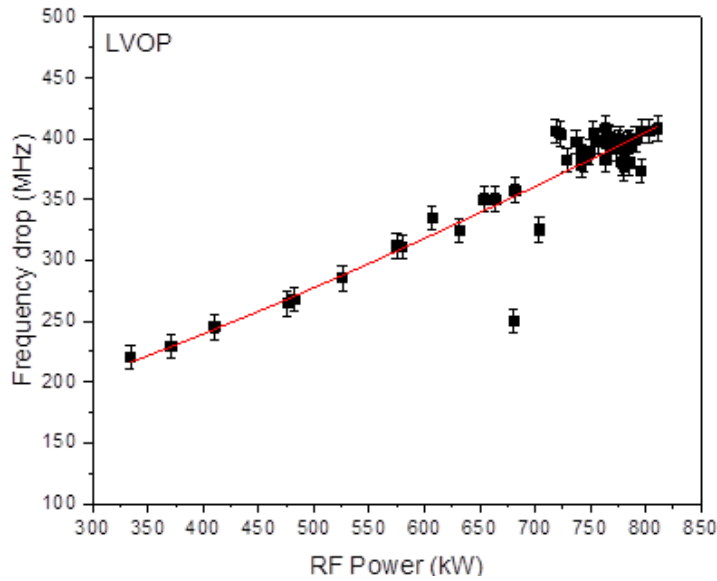


Fig. 1.2.28: Frequency drop with respect to the generated RF power.

Parasitic oscillations during CW operation

For most of the operating points in CW operation of the tube there was minor activity in the filter-bank channels. In detail at the most conditioned operating point of -2° there is no other signal than the one of the nominal mode, except if we decrease the beam radius to values as low as 9.45 mm. For this operating point (-2° , 9.45 mm) there is a visible signal in the filter-bank channel that covers the frequency range 159 GHz to 161 GHz, which, however, decays and vanishes after approximately 500 ms (Fig. 1.2.29). This signal is more persistent and remains visible for the complete duration of longer pulses when changing the gyrotron operating point to (-3° , 9.50 mm).

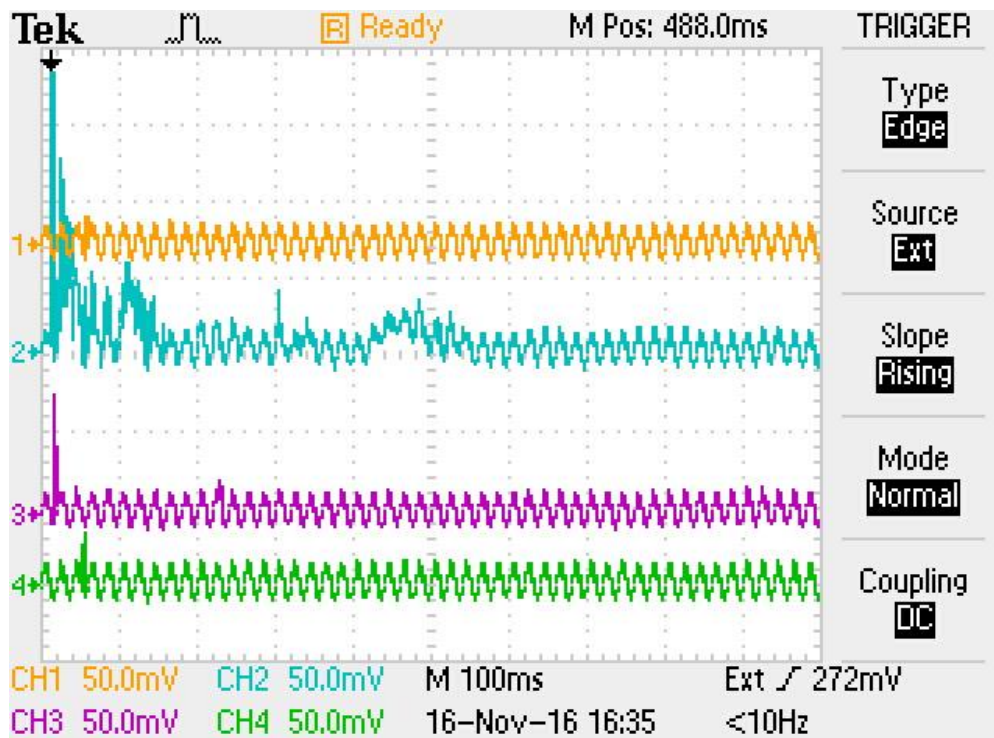


Fig. 1.2.29: Decay of the parasitic signal (blue) in the filter-bank after 300 msec.

Energy consumption

The scientific assessment of the experiment is based on pulses with total duration of approximately one hour. At the time of writing this report this sum includes eight 180 s pulses that were performed in series in order to verify that the three minute limit has been successfully and reproducibly achieved. The distribution of the duration of the pulses that are used in the scientific assessment of the CW operation of the industrial prototype gyrotron is presented in Fig. 1.2.30. In this histogram there are two primary peaks at 30 s and at 60 s. The reason that these two pulse duration were selected was to minimize the waiting time between pulses in order to speed up the search procedure for the optimal operating parameters. Of course much more pulses were performed, the total pulse duration in CW operation is approximately four hours. The filament heating was activated for approximately 417 hours.

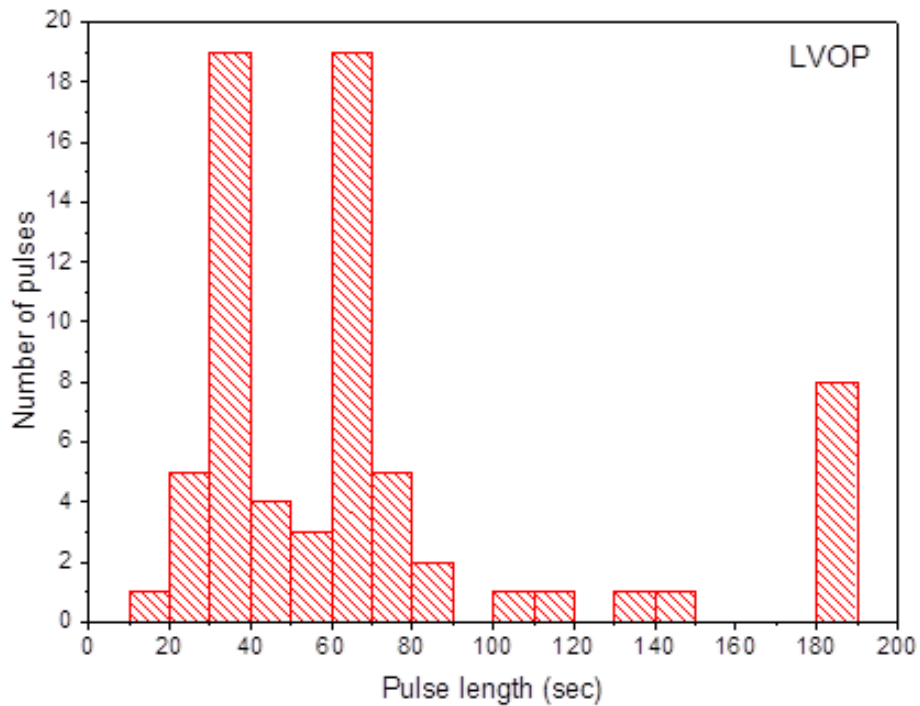


Fig. 1.2.30: Histogram of the duration of the pulses used for the scientific assessment.

High Voltage operating point

Due to maximizing the effort for optimizing the performance of the gyrotron for the LVOP, limited time was spent in CW operation of the tube at the High Voltage Operating Point (HVOP). Similarly to the LVOP and in order to minimize the waiting time between consequent shots, mostly pulses with duration 30 s and 60 s were performed, as it is visible in Fig. 1.2.31 where a statistical analysis of the pulse duration is presented.

At the HVOP the gyrotron was mainly operated with the magnetic field angles at the emitter region -2° and -3° and beam radii 9.50 mm and 9.55 mm. Fig. 1.2.32 summarizes the achieved output power and the corresponding efficiency for the attempted operating points. It is evident that in most cases approximately 800 kW were generated with the corresponding efficiency around 35 %. Although the operational time for the HVOP was significantly lower than for LVOP it can be concluded that the performance and limitations of the tube was very similar.

Fig. 1.2.33 presents the frequency drop with respect to the generated RF power as it was recorded in the HVOP. The situation is not much different from the LVOP resulting to approximately 400 MHz frequency drop for power in the range of 800 kW.

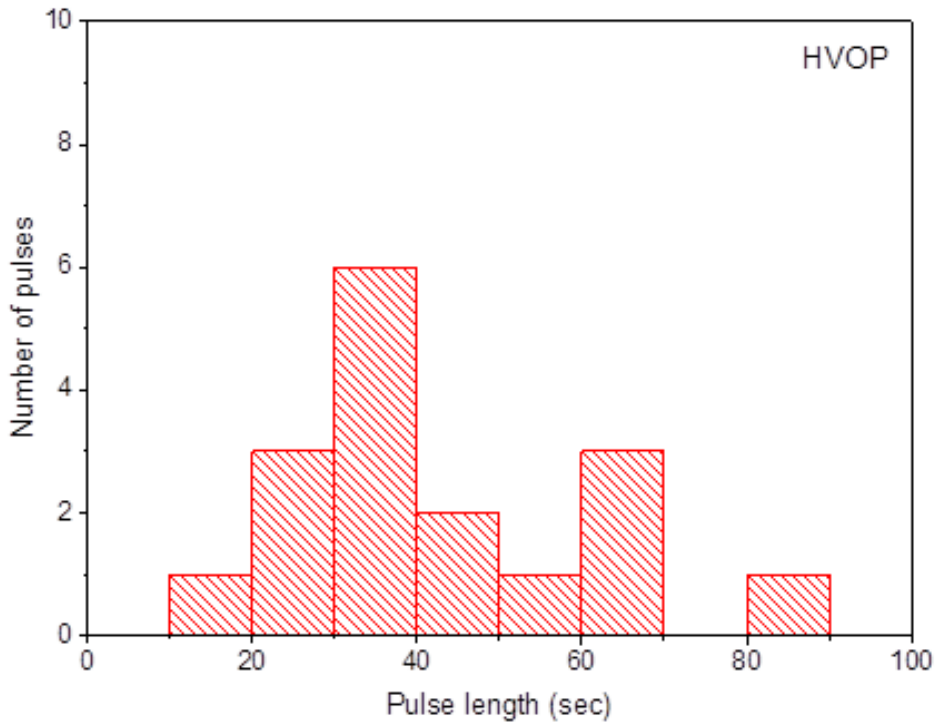


Fig. 1.2.31: Histogram of the duration of the pulses used for the scientific assessment.

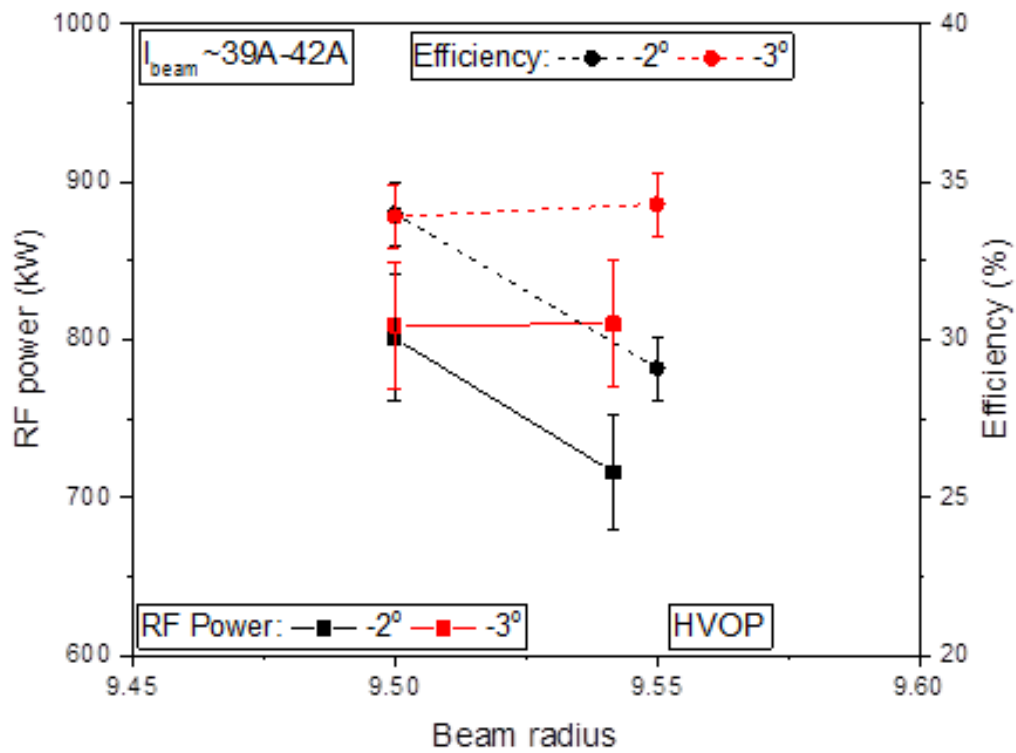


Fig. 1.2.32: RF power and corresponding efficiency at different operating parameters at the HVOP.

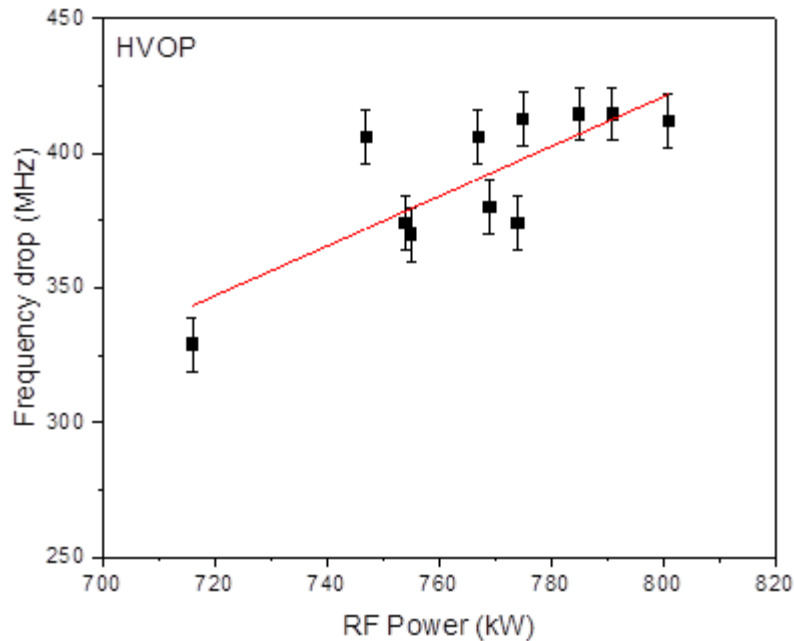


Fig. 1.2.33: Frequency drop with respect to the generated RF power at the HVOP.

1.2.6 Summary

The 1 MW, 170 GHz CW industrial prototype gyrotron, which has been developed by the European GYrotron Consortium in cooperation with the industrial partner Thales Electron Devices (TED) and under the coordination of the European domestic agency F4E, has been delivered at KIT on January 18, 2016. Since then, the gyrotron has been thoroughly tested, at different operating points in terms of accelerating voltage, beam current and magnetic field profile, both in the SP and LP regime with pulses up to 180 s.

Operation of the CW gyrotron with millisecond pulses resulted in stable excitation of the nominal mode at 170.22 GHz for a wide range of operating parameters and with a level of stray radiation comparable with the SP version of the tube. The Gaussian mode content of the RF beam was found to be at least 97 %.

In the SP regime and after optimization of the alignment of the gyrotron as well as of the operating parameters, it was possible to generate RF power in the 1 MW level. In detail with near nominal parameters, the highest obtained power was 930 kW with efficiency approximately 25 %. By increasing the electron beam current higher than the nominal parameters, namely $I_b = 53$ A with accelerating voltage $V_a = 78$ kV, power as high as 980 kW was achieved with slightly lower efficiency.

After proper conditioning of the tube with and without RF (which lasted approximately seven weeks), the experiments were continued in the LP regime with 180 s long pulses, which is the maximum possible with the available HV power supply at the KIT test facility. The maximum achieved power in 180 s pulses with nominal operating parameters is 786 kW with 37.2 % total efficiency, in depressed-collector operation. In detail the cathode voltage was 47.6 kV, the body voltage 24.6 kV and the average beam current 44.4 A. There were multiple cases where the generated power was slightly higher than 800kW, yet with pulses of 60s. It should be noted that the pulse duration was reduced in order to reduce proportionally the waiting time between pulses, which for the case of 180 s pulses is half an hour.

The experiments with the industrial prototype will be continued at EPFL Lausanne during 2017, whereas additional experiments with the SP tube will be performed in parallel at KIT in order to better understand the performance of the CW gyrotron and identify ways to further optimize the generated power.

1.3 Numerical Simulations

1.3.1 Design approaches for new multi-stage depressed collectors

A design approach for the collection of a sheet electron beam is proposed (shown in Fig. 1.3.1). Based on several considerations, analytical equations have been extracted for the design optimization and the estimation of the collection efficiency. This type of collector is appropriate for devices which operate with a sheet beam confined by a strong magnetic field, such as a free-electron laser (FEL) or a sheet-beam gyrotron. In order to apply the proposed design approach to conventional gyrotrons, the transformation of the cylindrical hollow beam to one or more sheet beams is proposed using appropriate magneto-static fields. A conceptual design for a gyrotron MDC system based on that idea is proposed. In order to illustrate this idea, two preliminary slightly optimized designs were simulated with efficiencies 80 % and 86 %.

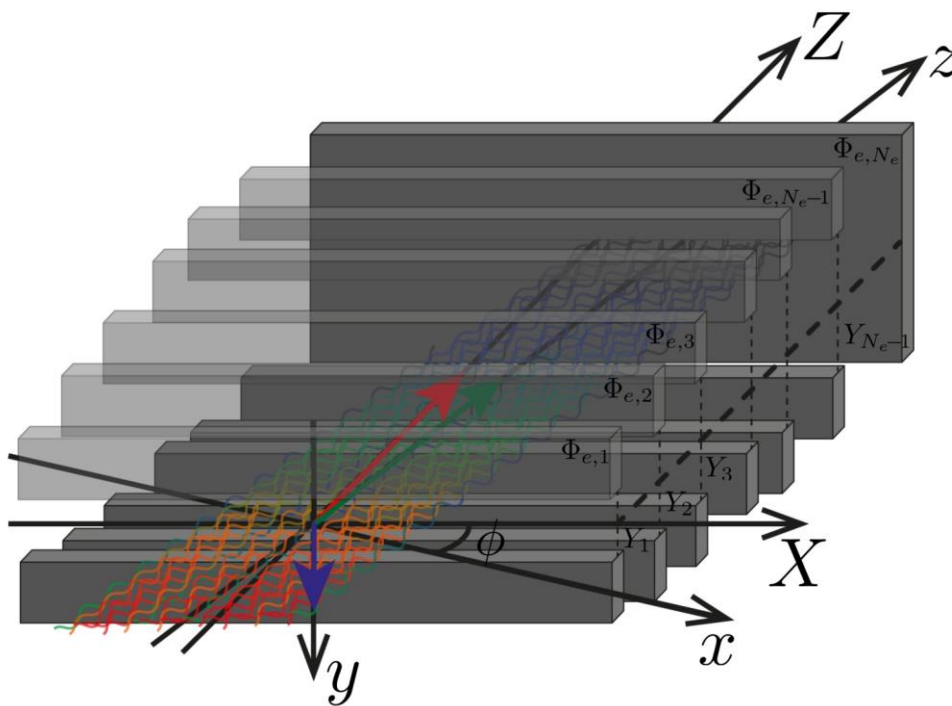


Fig. 1.3.1: Conceptual drawing of the proposed multistage depressed collector for sheet electron beam.

1.3.2 Influence of trapped electrons on the gyrotron performance

The presence of trapped electrons in the MIG region can cause many problems to the gyrotron operation such as decreased efficiency, failure of the excitation of the nominal operating mode at the cavity, voltage stand-off instabilities, parasitic oscillations, and increased stray radiation level. Several issues related to the two types of electron trapping mechanisms which can take place in gyrotrons were studied. Two MIG design criteria were proposed for the suppression of electron trapping in order to minimize the risk of possible problems. The major advantage of the proposed design criteria is that checking whether a design satisfies them or not is an easy and quick process requiring just a self-consistent electrostatic trajectory simulation code. The importance of the design criteria was also demonstrated by comparison and analysis of the experimental results of three different high power gyrotron tubes. Finally, several empirical design principles were defined for the satisfaction of both criteria. Influence of manufacturing tolerances in the emitter ring region.

An important sensitivity of the electron beam parameters of a MIG to the manufacturing imperfections in the emitter ring region has been demonstrated. In particular, it has been shown that not only the velocity spread can be significantly increased due to emitter ring imperfections but also the average pitch factor which can influence the mode excitation and the interaction efficiency at the gyrotron cavity. Furthermore, the formation of harmful long tails in the pitch factor distribution was also observed. This sensitivity can theoretically explain possible stochastic behavior of gyrotron tubes with identical scientific designs. It has also been shown that this sensitivity becomes more critical for thinner emitter rings. A factor has been defined for the quantification of the sensitivity. Furthermore, the influence of a possible misalignment of the emitter ring with respect to its neighboring parts on the pitch factor distribution has been analytically investigated. Then, a possible solution of this major issue for the gyrotron MIG designs was proposed by introducing anti-emission regions on the two ends of the emitter ring as shown in Fig. 1.3.2. Using this idea, it was possible to significantly decrease the sensitivity factor. In addition, an alternative approach was proposed for the cases in which a conventional emitter is used in order to suppress the harmful long tails in the pitch factor distribution.

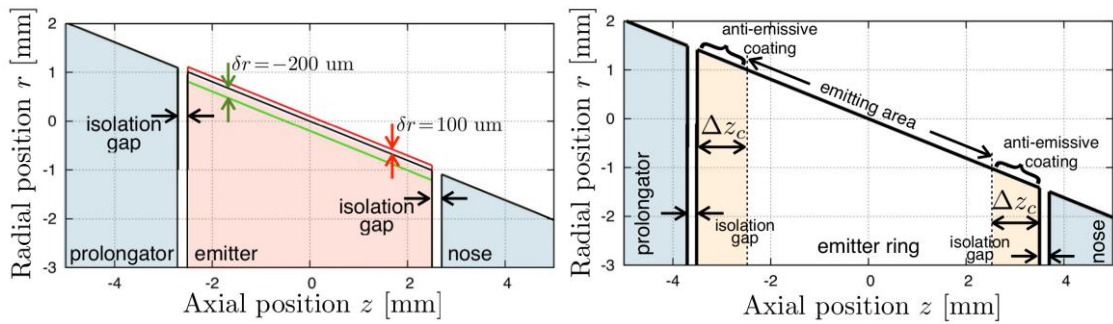
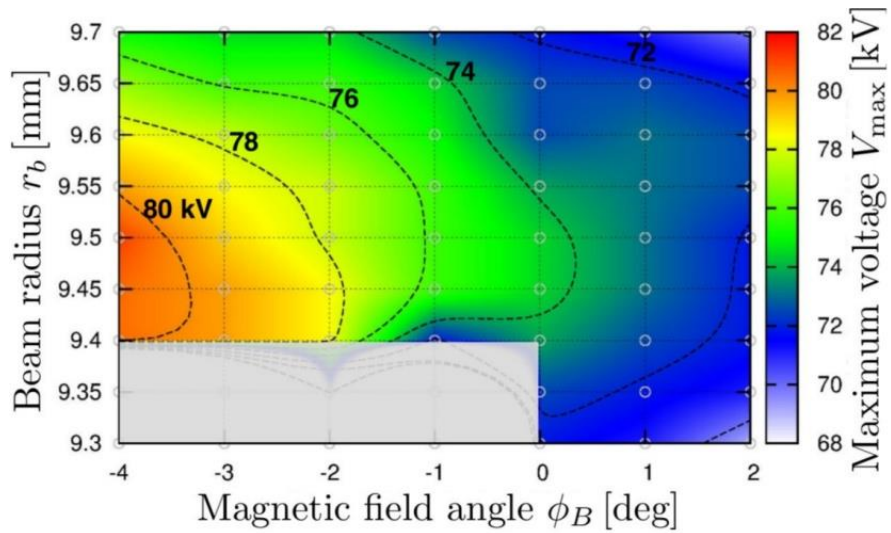


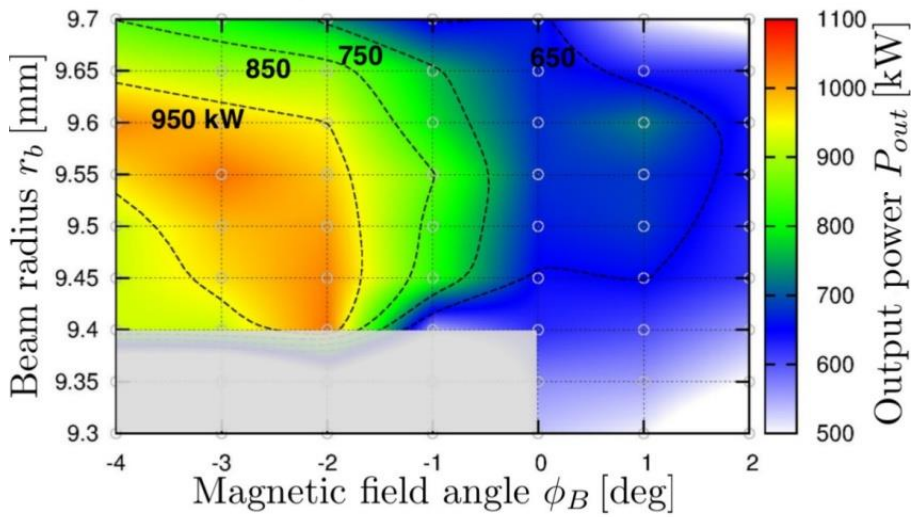
Fig. 1.3.2: Conventional (left) and the proposed type (right) of emitter ring which significantly decrease the sensitivity in the manufacturing tolerances.

1.3.3 Magnetic profile analysis

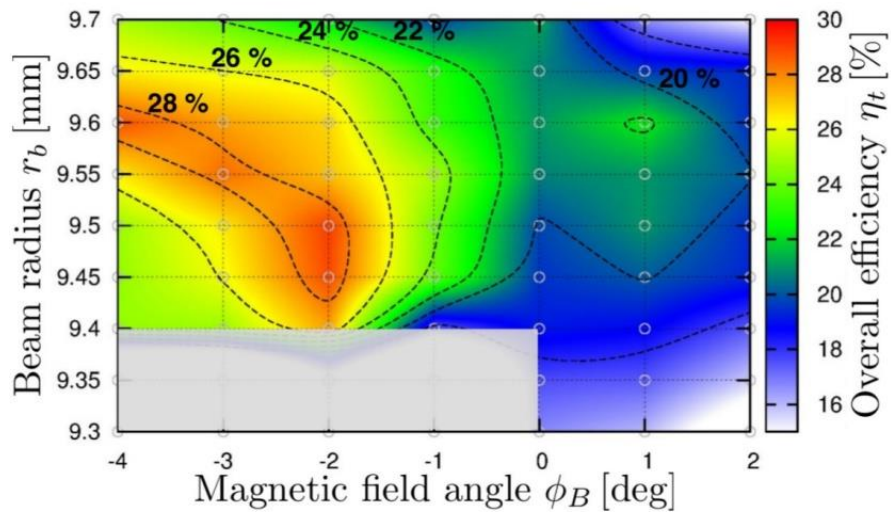
A simple analytical technique was proposed for the definition of the magnetic profiles used in the gyrotron experiments by three important parameters for the interaction and the beam quality instead of the arbitrary currents of the coils of the magnetic system. These parameters are (i) the magnetic field at the cavity, (ii) the beam radius at the cavity, and (iii) the angle of the magnetic field at the emitter. It was theoretically and experimentally demonstrated that two magnetic profiles are equivalent in terms of beam-wave interaction if the magnetic profile parameters are the same. Theoretical and experimental maps (see Fig. 1.3.3) were assembled in the magnetic profile parametric space for the SP prototype of the EU 170 GHz 1 MW CW gyrotron project. Many interesting conclusions were extracted while the magnetic profiles for the optimal operation of the tube were identified. Finally, it should be mentioned that the proposed methodology has been established as a standard procedure of the experimental investigation of the gyrotrons at IHM, KIT.



(a) Maximum voltage



(b) Output power



(c) Overall efficiency w/o depressed collector

Fig. 1.3.3: Operational maps of the short-pulse prototype of the 1 MW Gyrotron.

1.3.4 Investigation of the impact of tolerances on quasi-optical system

The first experiments with the EU 1 MW 170 GHz CW industrial prototype gyrotron for ITER have been completed in 2016. The mirror system in the CW gyrotron has been modified by reducing the thickness of the three mirrors by 200 μm . It is found that there are some misalignments in the 1st, 2nd and 3rd mirrors. The field distribution in the quasi-optical (QO) mode converter has been analyzed using SURF3D, and the simulation results show a good agreement with the long pulse high power experiment. Fig. 1.3.4 shows the field distribution at 0.25 m away from the gyrotron window.

The impact of tolerance on QO systems has been investigated. The possible fabrication errors of the launcher and the misalignment in the mirror system have been included in the analysis. For the mirror system in the EU ITER gyrotron, in order to keep the stray radiation in the quasi-optical mode converter to be <5 %, the deviation of the direction of the vector normal to the mirror surface should be smaller than 0.2° for each mirror.

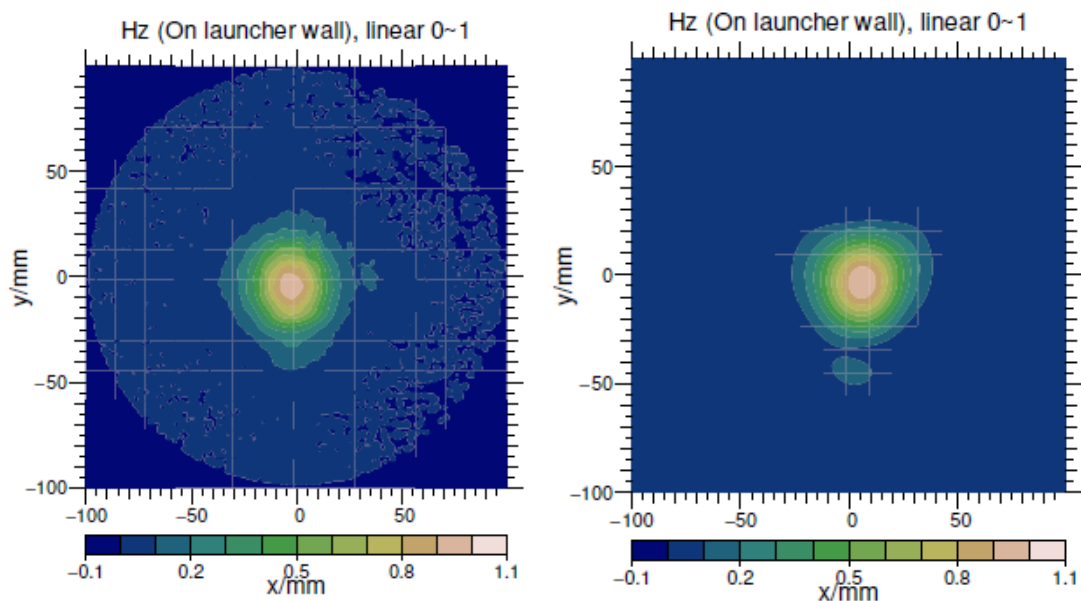


Fig. 1.3.4: The field distribution at 0.25 m away from the gyrotron window: experiment (left) and simulation (right).

1.3.5 Design of the quasi-optical mode converter and MOU for TCV gyrotrons

A quasi-optical (QO) mode converter has been designed for the dual-frequency TCV gyrotrons. The TCV gyrotrons will be operated at 84 GHz and 126 GHz, respectively. The simulation results show that the Gaussian mode contents are 98.74 % and 97.7 %, and the stray radiations are 3.42 % and 2.18 %, for the operation at 84 GHz and 126 GHz, respectively. A prototype of MOU for the TCV gyrotron has also been designed to transform the Gaussian-like distributions into an HE_{11} mode. The simulation results show that the conversion efficiency is quite sensitive to the parameters of the RF beams. It is impossible to achieve high conversion efficiency for both RF beams transformed in the same MOU mirror system.

A new subroutine for the transformation of the local coordinates of mirrors into the global coordinate system has been developed and integrated into the TWLDO code, and the global coordinates of the mesh points can be directly used as the input data for the SURF3D computer code. A subroutine for the propagation of the HE_{11} mode on the launcher wall has also been developed.

1.3.6 Development of a tool for the simulation of electromagnetic fields in quasi-optical systems of gyrotrons

Within the scope of a master thesis a simulation tool for the full wave calculation in quasi-optical (QO) mode converters based on the electric field integral equation (EFIE) was developed. The goal was a new, fast simulation tool, with a good scaling for highly oversized geometries and higher flexibility than available commercial tools. That provides a basis for further research and the development of new synthesis methods for QO systems. The mode converter separates the electron beam from the RF beam and transforms the cavity output, a high order cavity mode, to a fundamental Gaussian mode. Because of the high energy output and the continuous wave operation of gyrotrons used in fusion experiments, it is important to design very efficient quasi-optical mode converters with low stray radiation and a high Gaussian beam content in the output field. The developed simulation tool allows a full wave simulation of the electromagnetic fields in QO systems, based on the EFIE.

As a first example in Fig. 1.3.5 the simulation result for the QO system of the W7-X gyrotron is shown. The QO system consists of a launcher and three mirrors with a total area of $24700 \lambda^2$, where λ is the wavelength at 140 GHz. Therefore, the QO system is highly oversized which is a challenge for every full-wave simulation method. Because of the high order method used in our simulation tool, the required number of unknowns for an accurate simulation can be reduced to $6 \cdot 10^5$ and we are able to simulate the whole system in only 90 minutes.

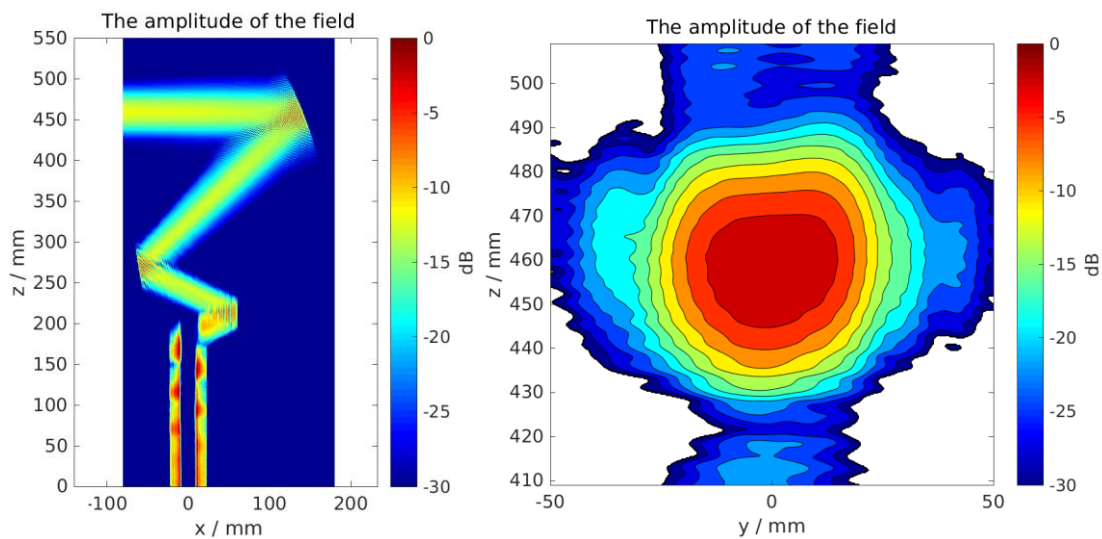


Fig. 1.3.5: Simulated electric field of the QO system for the W7-X gyrotron, in the x-z-plane (left) and at the output window (right).

1.4 Inverse Magnetron Injection Gun

1.4.1 Introduction

Gyrotrons are the unique RF sources which satisfy the exceptional requirements for ECRH of present and future fusion power plants. Previous experiments have already shown the operation of gyrotrons with an RF output power in the MW range, operating frequencies up to 170 GHz, and pulse lengths of several seconds up to continuous wave (CW). However, future nuclear fusion devices such as DEMO will require the development of gyrotrons with even higher frequencies (in the range from 200 GHz up to 300 GHz) at excellent efficiencies and multi-MW levels of RF output power in CW operation. To prevent mechanical

launcher steering, frequency step-tunable RF sources will be required for localized plasma stabilization. In order to fulfill the demanding requirements regarding increase of frequency and RF output power, an Inverse Magnetron Injection Gun (IMIG) has been designed and is under construction for the KIT 2 MW coaxial cavity gyrotron. This new IMIG (see Fig. 1.4.1) shall show the way towards a more robust operation at even higher output power levels. That shall be achieved by the implementation of a larger emitter ring, by doing a better post processing and by having significantly improved cooling conditions. Considering the fundamental beam and operating parameters, an excellent beam quality has been achieved in the simulations which results in a very low velocity spread. In addition, the IMIG fulfils the gun design criteria, which are published in and trapped electrons are suppressed in a much simpler way compared to the “conventional” MIG used in today’s gyrotrons. Adapted from the triode configuration, the presented IMIG can also be operated in conventional hollow cavity gyrotrons as well as in the new KIT coaxial long pulse gyrotron under the fulfillment of the already mentioned gun design criteria.

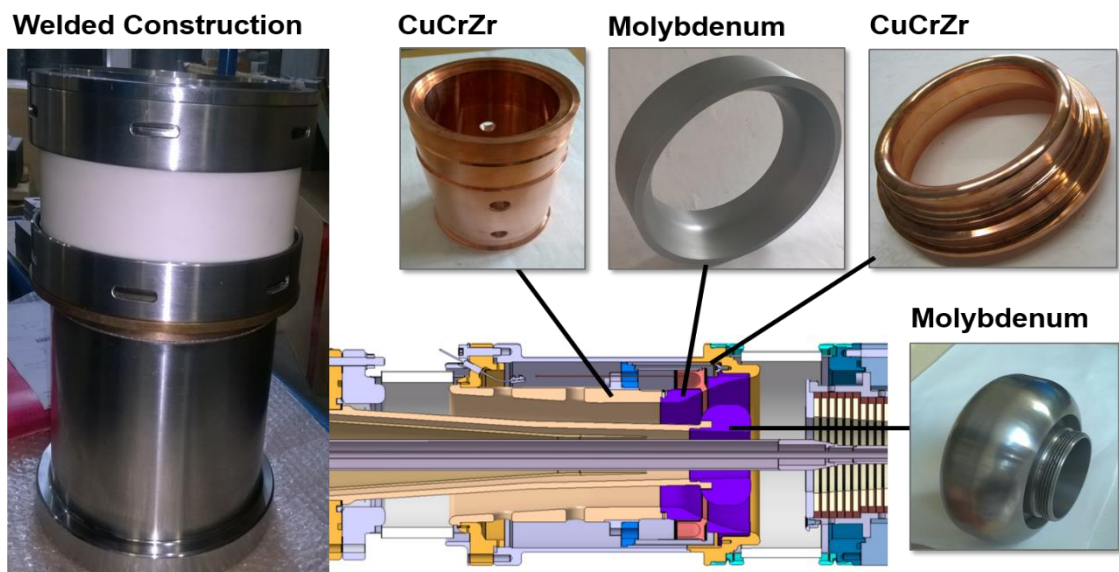


Fig. 1.4.1: 3D sketch of the Inverse Magnetron Injection Gun (IMIG) and the already manufactured subcomponents.

In the present design the emitter radius was fixed to 62 mm with a longitudinal emitter thickness of 5 mm. The emitter is slanted at an angle of 25 degrees with respect to the axis of the tube. The emitter is thermally isolated from the neighboring regions by the use of isolation gaps at both sides with a width of 200 μm . Due to the isolation gap an electric field enhancement is generated at the edges of the emitter. Hence, the emitter is embedded into the cathode structure by 70 μm .

The most important requirement of a MIG is the generation of a hollow helical electron beam with a high quality. Therefore, the design and tolerances of the beam forming components play an important role in the generation of a high quality electron beam. The displacement of the beam forming components is determined by (i) thermal expansion of the components during operation and (ii) by the manufacturing tolerances. The first item can be avoided by the consideration of the thermo-mechanical behavior, improved cooling conditions and the use of material compositions with high thermal conductivity.

The influence of the manufacturing tolerances (item ii) of the beam forming components regarding the beam quality will be explained and discussed in this paper. Furthermore, this work gives an estimation of the maximum permissible displacement of the main IMIG components. Therefore, a new mechanism for the investigation of three dimensional (3D) displacements of beam forming components will be proposed and presented.

1.4.2 Tolerance Study of the IMIG

The alignment and coaxiality of the anode, the position in the warm magnet borehole as well as the temperature distribution of the emitter has a significant influence on the quality of the electron beam, and therefore on the generated output power and efficiency. In the following, the influence and suppression of the mentioned tolerances will be discussed and benchmarked by the help of the simulation tool Ariadne.

Anode Misalignment

One of the most important criteria for a high-quality electron beam, is an homogenous distribution of the electric field strength at the emitter surface and therefore a perfectly aligned anode is required. Due to the large size of the anode (see Fig. 1.4.1) and the summation of all the mechanical tolerances, the correct alignment of the cathode to the anode is a critical issue and has to be minimized for mechanical implementation. In order to estimate the maximum allowable anode deviation, 3D simulations are required. Due to the fact that there is a 3D code missing to simulate the shifted geometry, a transformation of an 2D model into an 3D model was disposed. For this purpose, the anode was radially shifted in $5\ \mu\text{m}$ steps in a range of $\pm 500\ \mu\text{m}$ ($d_1 \dots d_n$), which is shown in Fig. 1.4.2. For each distance the corresponding beam parameters were calculated and stored in a separate file. Subsequently, the different distances of the misaligned anode to the emitter were transformed into the 3D model and the resultant 3D beam parameters were recalculated. In Fig. 3d it is shown that the misaligned anode has no significant influence to the average pitch factor, however the pitch factor spread is increasing from 6.0 % ($0\ \mu\text{m}$) up to 10 % ($500\ \mu\text{m}$). With increasing anode misalignment, the pitch factor distribution is becoming wider (Fig. 3 b-c, blue colored). Assuming a thermal isolation gap of $300\ \mu\text{m}$ instead of $200\ \mu\text{m}$ the emitter is much more sensitive regarding the misalignment of the anode and the resultant beam parameters. Compared to the nominal gap width ($200\ \mu\text{m}$) the pitch factor distribution at $300\ \mu\text{m}$ (Fig. 1.4.3, red colored) is significantly wider for all radial anode deviations. Hence, the amount of electrons with higher pitch factor is increasing with increasing misalignment of the anode. With an anode misalignment of more than $300\ \mu\text{m}$ the pitch factor exceeds the value of 2.2 which is more than the maximum allowable pitch value. Therefore, the generation of trapped electrons is starting and the generation of a Halo current will proceed. For the manufacturing process the presented tolerances were considered. A maximum gap width of $200\ \mu\text{m}$ will be maintained in hot condition due to the consideration of the thermomechanical simulation results and the improved cooling conditions of the cathode by the use of advanced material compositions. Furthermore, the deviations of the anode will be smaller compared to a 'conventional' MIG, which is achieved by doing post processing after the brazing and welding process and by having significantly improved cooling conditions of the anode.

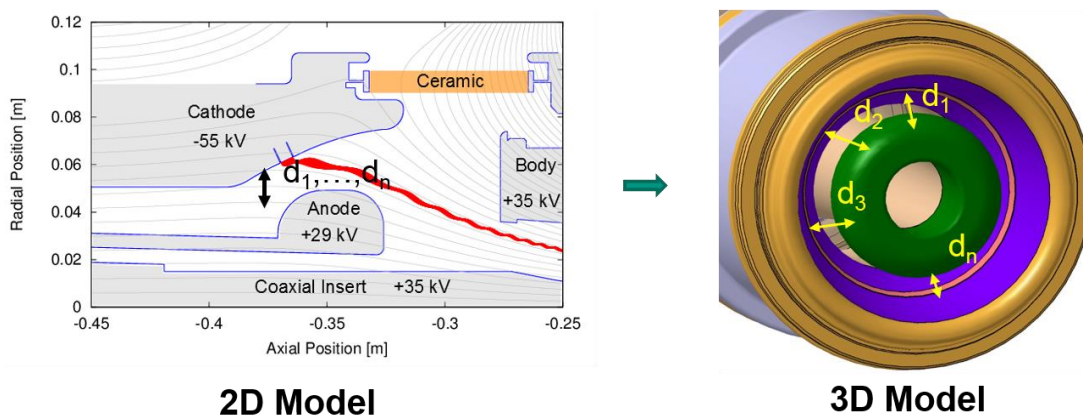


Fig. 1.4.2: Transformation procedure of the 2D into 3D model.

Emitter Misalignment

The radial emitter misalignment has also a significant contribution to the quality of the hollow electron beam. This radial misalignment is mostly related to a deviating emitter temperature and therefore a smaller or larger expansion of the emitter unit. In the following, the radial emitter displacements in the range of -150 μm up to +150 μm were investigated. The underlying assumption is a homogenous deviation over the full azimuthal emitter area. The definition of the positive and negative direction is shown in Fig. 1.4.4. The radial deviation of the emitter causes (i) a variation of the average pitch factor and (ii) a significant pitch factor variation of electrons which are emitted from the rear part of the emitter. In the nominal case (emitter deviation of 0 μm) the average pitch factor is 1.3 with a minimum spread of 6.0 % and a linear behavior over the investigated range, shown in Fig. 1.4.5. For a negative deviation of -150 μm the average pitch factor represents a value of 1.08, while the pitch factor at +150 μm amounts 1.58 with a spread of 10 % and 15.5 %, respectively.

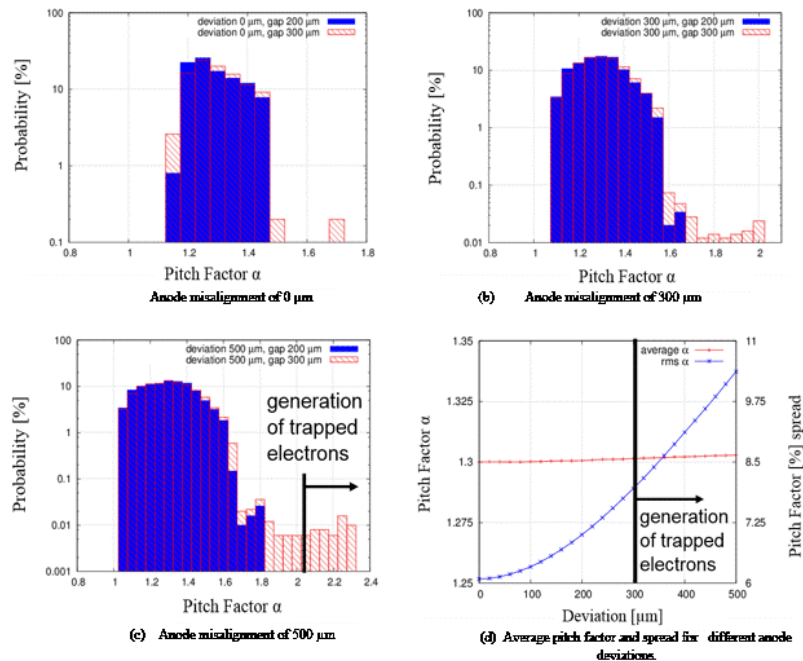


Fig. 1.4.3: Pitch factor distribution for different anode misalignments (a-c) with a gap width of 200 μm (nominal case, blue colored) and 300 μm (red colored), (d) describes the average pitch factor and spread for anode deviations in the range of 0 μm to 500 μm with a gap width of 200 μm .

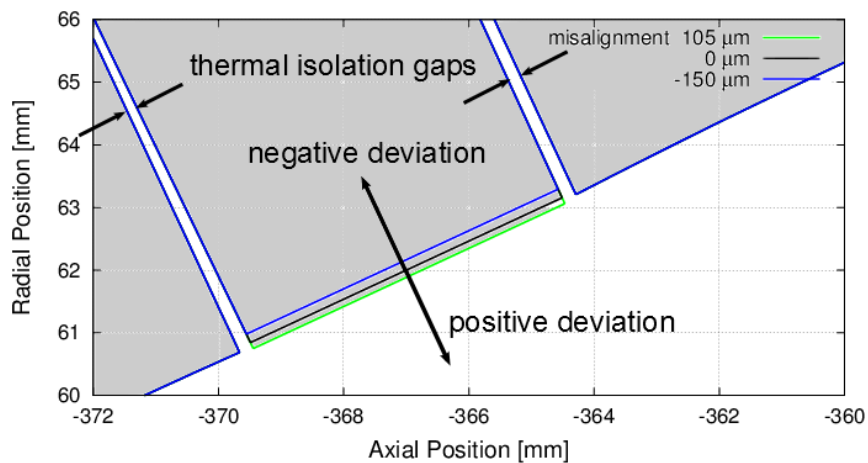


Fig. 1.4.4: Definition of the emitter deviation and representation of the thermal isolation gaps.

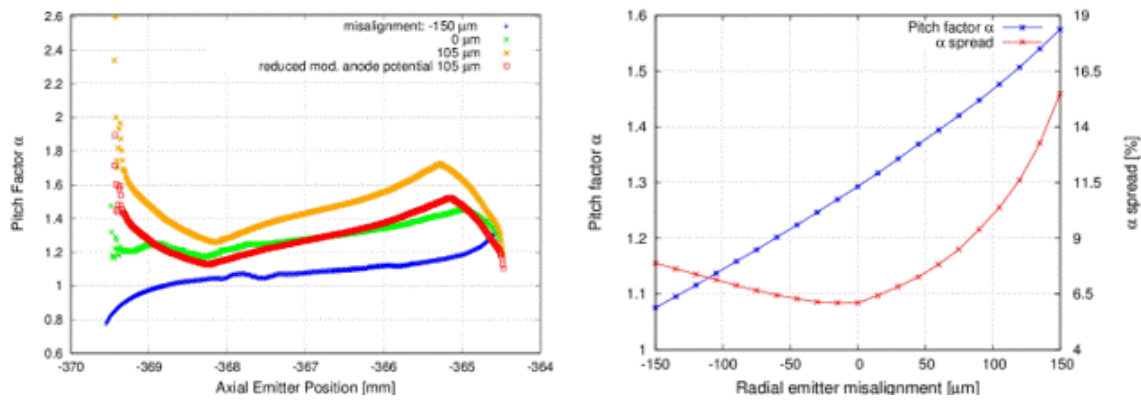


Fig. 1.4.5: Left: Pitch factor at the cavity as a function of the emitting point along the emitter surface for different radial misalignments. Right: Pitch factor and RMS α spread at the cavity center, regarding the radial misalignment

In particular, if the deviation is getting positive, the pitch factor of the electrons emitted from the rear part is increasing significantly and exceeds 2.6 for a misalignment of +105 μm , while for negative deviations the pitch factor of these electrons is decreasing. This effect is related to the strong variation of the electric field at the rear part of the emitter. The “edge effect” can be significantly reduced by the help of the modulation anode. Under the assumption of an average pitch factor of 1.3 and an emitter misalignment of 105 μm , the modulation anode potential has to be reduced from 29 kV (nominal case) to 26.5 kV. The pitch factor distributions for both cases are shown in Fig. 5a (orange and red color). It can be seen that the pitch factors of the electrons emitted from the rear part are reduced from 2.6 to 1.9, which is below the maximum pitch factor limit. Hence the misalignment of the emitter can be much easier compensated compared to the Magnetron Injection Guns which are currently used.

Temperature Inhomogeneity at the Emitter Surface

The emission inhomogeneity of the gyrotron emitter depends mainly on the homogeneity of (i) the surface roughness, (ii) the BaO-layer, (iii) the electric field distribution and (iv) the temperature distribution. Those electron beam in-homogeneities create a non-uniform beam and an increase in the velocity spread of the emitted electrons. Measurement of the Current-Voltage characteristics is a simple and fast method to determine the emission inhomogeneity. The main contribution to the inhomogeneity of the electron beam is a non-uniform temperature distribution.

The temperature measurement of the inverse emitter at 1000 $^{\circ}\text{C}$ has shown an excellent temperature distribution of $\pm 7^{\circ}\text{C}$, which is 46 % less compared to a currently used MIG emitter. Under consideration of the temperature inhomogeneity the simulated pitch factor spread is slightly increasing from 6.5 % up to 6.7 %, shown in Fig. 1.4.6. With increasing temperature deviation the average pitch factor remains constant, while the spread is increasing to 10 % at $\pm 27^{\circ}\text{C}$. The inhomogeneity of the temperature distribution has also a significant influence on the kinetic energy distribution. In Fig. 7 the kinetic energy of 20200 simulated electrons versus the azimuthal position in the cavity for a deviation of $\pm 0^{\circ}\text{C}$ (red colored) and $\pm 7^{\circ}\text{C}$ (nominal case, blue colored) can be seen. In case of $\Delta T = 7^{\circ}\text{C}$ the kinetic energy is lower in the regions of high temperatures, because the space charge is higher and therefore the resultant electric field lower. Consequently, the kinetic energy is higher at regions with lower temperature. As a result, the maximum decelerating voltage at the single stage depressed collector has to be reduced to the energy of the slowest electron, which decreases the overall gyrotron efficiency.

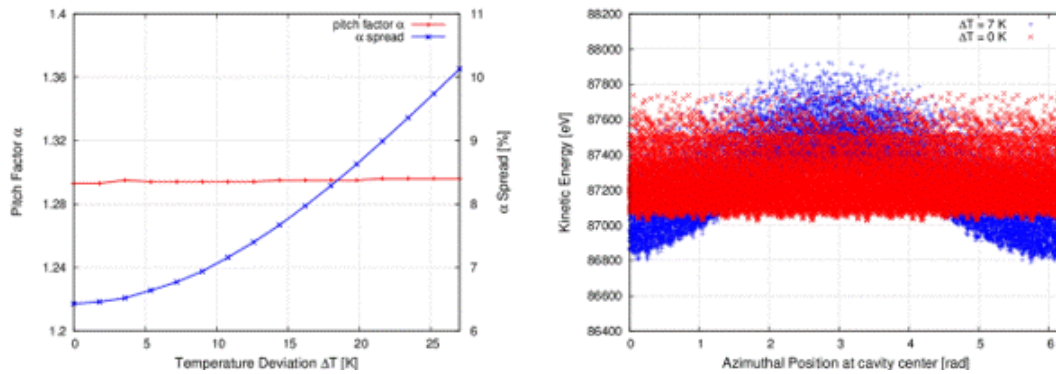


Fig. 1.4.6: Left: Pitch factor and RMS α spread simulated at the cavity center for different temperature deviations. Right: Kinetic energy as function of the azimuthal position at the cavity center for emitter temperature deviations of 7 K (blue points) and 0 K (red points).

Summary

In this work, the tolerance study of the Inverse Magnetron Injection Gun (IMIG) appropriate for the KIT coaxial-cavity gyrotron has been presented. The results have shown the dependency between misalignments, manufacturing tolerances, temperature distribution and the electron beam parameters, mainly the pitch factor and its RMS.

The work has also shown that the misalignment of the emitter, anode as well as the isolation gap has a significant contribution to the excitation of an electron beam halo and consequently the generation of low frequency oscillations. Therefore, the maximum acceptable displacement of each component has been presented in order to guarantee a stable gyrotron operation. It has been figured out, that the sensitivity of the IMIG is lower compared to the currently used 'conventional' MIGs and shows great promise for a stable operation without the generation of trapped electrons.

Additionally, the effect of emitter temperature inhomogeneity regarding the beam quality has been investigated based on IR-measurements.

Furthermore, the components were already manufactured with an excellent surface quality, taking into account the calculated permissible tolerances. Furthermore, excellent welding and solder joints for perfect vacuum conditions have been achieved.

1.5 EUROfusion: Research and Development towards a Gyrotron for future DEMO

1.5.1 Design and manufacturing of active-cooled subcomponents for a longer pulse 170 GHz, 2 MW coaxial-cavity gyrotron

Performance requirements for the gyrotrons for DEMO are operating frequencies above 200 GHz and output powers of 1-2 MW. Coaxial-cavity gyrotrons with inner conductor offer some advantages in comparison to conventional gyrotrons with a hollow circular waveguide cavity. Therefore, gyrotrons of coaxial-cavity type are a promising option for future fusion applications, and especially a promising solution for the operation at DEMO.

Impressive experimental results obtained with the KIT 2 MW, 170 GHz short-pulse coaxial-cavity pre-prototype have shown the large potential of the coaxial concept in the multi-MW operation regime.

Therefore, the main focus is the development and verification of a 2 MW, 170 GHz longer-pulse coaxial gyrotron with a pulse length up to a few seconds. This verification of the coaxial concept at longer pulses will open the path towards a mature coaxial gyrotron technology for DEMO.

In order to increase the gyrotron pulse length of the 2 MW coaxial cavity gyrotron all components have to be equipped by active cooling systems. The example of the conceptual design is shown in Fig. 1.5.1. One of the main requirements is the conservation of the modularity of the gyrotron. The concept is based on an independent cooling system implemented for each component. At a first step, the launcher, cavity and beam tunnel, are optimised for longer-pulse operation. The modifications will be described in the following and are shown in Fig. 1.5.2. Start of operation of the Coaxial Longer-Pulse Gyrotron is planned for the middle of the year 2017.

Launcher: The launcher together with the mirror system is responsible for the conversion of the main $TE_{34,19}$ mode into a fundamental Gaussian mode. During the mode conversion process the power loading at the launcher surface is very high. Especially the loading at the top part of the launcher and in the area of the launcher cut, where the complete RF-power is finally focused, is critical. In order to guarantee a stable operation also the top of the launcher will be cooled. This requirement meets some challenges, because the top part of the launcher is extended by 60 mm into the mirror box where no access for cooling pipes from outside of the gyrotron is possible. Therefore, the water entrance and outlet have to be supplied from the bottom and the water flow is implemented in a helix-like flow. At the top of the launcher, both helical channels will be connected in the so called "breakthrough". In lower regions of the launcher the channels go into "reservoirs", where the channels end. Due to the complex structure, the channels have to be milled with a 5-axis milling cutter. In order to seal the channels, a stainless steel cover will be imposed and welded from the outside of the launcher. Due to the fact that the launcher and cover consist of different materials that have different thermal extension coefficient, a bellow is necessary to compensate the forces. In 2016 the launcher was successfully manufactured with an excellent surface quality. Furthermore, excellent soldered and brazed joints with a leakage rate $<10^{-12}$ mbar l/s were achieved with different material compositions.

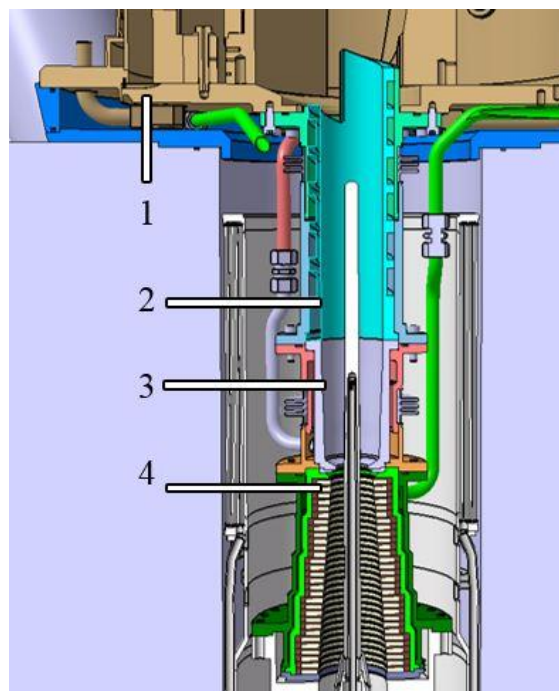


Fig. 1.5.1: Overview of the proposed cooling system for the most critical gyrotron subcomponents (1-mirror box, 2-launcher, 3-cavity, 4-beam tunnel).

Cavity: The cavity is the region where the RF power is generated due to interaction between the electrons and the RF field. The power loss at the surface of the cavity is 50 kW. The highest power loading ($\sim 2 \text{ kW/cm}^2$) takes place at the centre of the cavity (region with constant diameter). It leads to a very high temperature gradient at the inner cavity wall, which results in thermal stress and deformation. The frequency of the RF wave depends strongly on the diameter of the cavity and hence strongly on the deformation and thermal expansion. Therefore it is essential to implement a water cooling system for the cavity in the longer pulse operation regime. The approach of the active cooling system is similar to the design of the launcher. However, due to the position and orientation a helical channel system is not necessary. The different temperatures, material properties of the cover and outer cavity wall require also the implementation of a bellow. The reduction of the water cooling gap (see Fig. 1.5.2) increases the flow velocity of the water and therefore the cooling efficiency. The limitation for the cavity is a maximum temperature of approximately 350°C at the inner surface. In a *COMSOL* simulation the temperature of a pulse with duration of 500 ms was calculated. At the centre of the cavity a maximum temperature of 280°C was predicted. The non-linear uptaper of the cavity was also extended and optimised. The simulation results predict a transmission efficiency of 99.85 % of the $\text{TE}_{34,19}$ mode and a low mode conversion in the uptaper. The design of the cavity was finalized and the manufacturing has started.

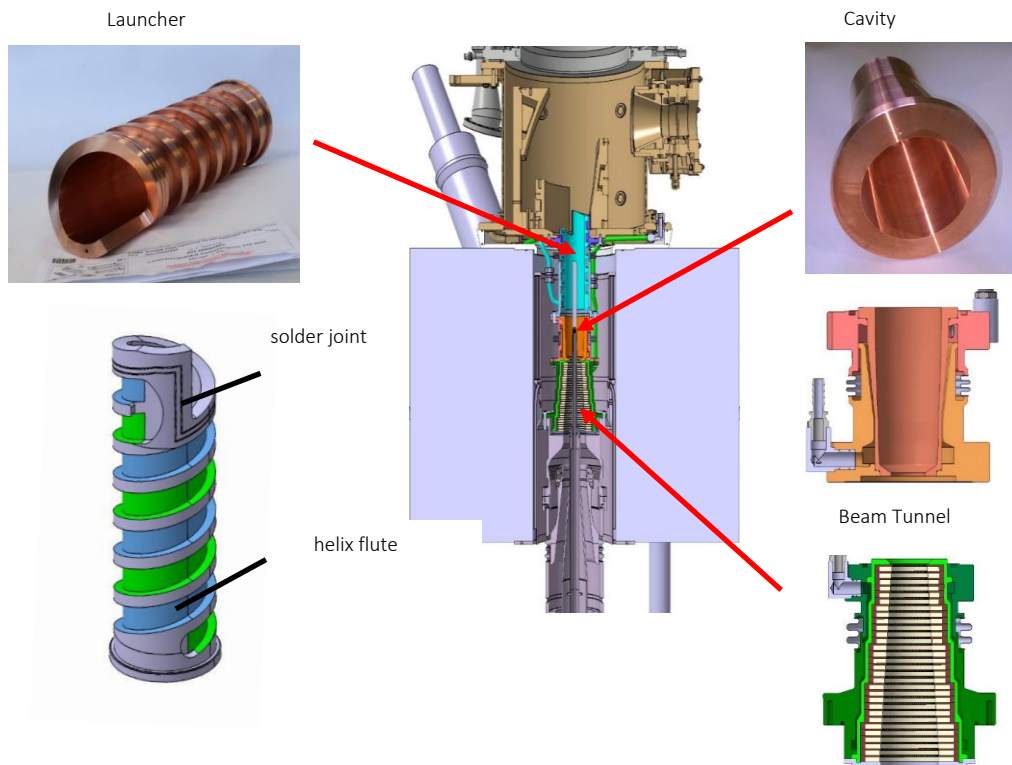


Fig. 1.5.2: Manufactured subcomponents of the coaxial long pulse gyrotron.

Beam tunnel: The beam tunnel consists of stacked copper and ceramic rings. The structure is very sensitive to the excitation of parasitic oscillations which might increase the power loading in the structure significantly (and destroy the good electron beam properties). Therefore an active cooling system is obligatory. Fig. 1.5.2 shows the construction of the beam tunnel including the water cooling system. An outer cover is also welded to the outside and forms with the outer metal layer an annular gap cooling. The subcomponents of the beam tunnel are already delivered and partly manufactured.

Mirror Box: In order to build a cost-effective gyrotron, the mirrors and the mirror box will be reused from an older industrial coaxial prototype gyrotron for ITER with slight modifications at the absorber ceramic,

collector, flanges, and window housing, in order to satisfy the requirements of the modularity. Currently, the mirror box is under preparation for the installation of the longer-pulse components. The water inlet for the beam tunnel, cavity and launcher is fixed at the bottom of the mirror box. Due to the fact that the gyrotron will operate in longer pulse operation it is necessary to bake it out at 350°C. Therefore, the water channels and connections have to be heat-resistant up to 350°C; hence metallic sealed components are required. In addition, a prototype metallic sealed water connection was made, which has shown excellent performance at the nominal operating water pressure.

1.5.2 Physical designs and tolerance studies of the key components for an 240 GHz gyrotron for DEMO

In-depth design studies of DEMO-compatible gyrotrons, starting with key components, are necessary to identify and overcome possible design and simulation obstacles and limitations. In order to obtain a full picture of such challenges, the two major concepts – conventional, hollow-cavity (or: cylindrical-cavity) and coaxial-cavity gyrotrons – are investigated in parallel in the frame of this work. Both gyrotron designs are based on the EUROfusion DEMO baseline 2012 (aspect ratio 4.0). However, most of the findings are applicable also to the updated DEMO baseline 2015 (aspect ratio 3.1). In 2016, the focus of work has been on fast frequency tunability (in steps of 2-3 GHz within roughly one second) and on multi-frequency operation (in leaps of 30-40 GHz without restrictions on tuning speed), as well as on tolerance studies. Investigations on output power maximisation (above 1 MW) with the conventional gyrotron concept were also performed. The coaxial-cavity design was optimised for good efficiency, while maintaining the technical boundary conditions at present-day conservative levels. The key parameters of the two designs are given in Table 1.5.1.

Table 1.5.1: Key parameters of the two gyrotron designs.

Parameters (ideal beams)	Coaxial Concept	Conventional Concept
Frequency (GHz)	237.5	236.0
Interaction mode	TE _{49,29} (Eigenvalue ≈ 158)	TE _{43,15} (Eigenvalue ≈ 103)
Beam Current (A)	69.3	43
Beam Voltage (kV)	85.6	61
Magnetic Field (T)	9.58	9.175
Output Power (kW)	1900	920
Interaction efficiency η_{elec} (%)	33	36

Coaxial-cavity 2 MW design

In 2014-2015, the basic coaxial-cavity design was finished, including multi-frequency compatible mode selection, cavity design with coaxial insert, Magnetron Injection Gun (MIG) based on a realistic magnet design, and initial concepts for the description of misalignments and nonuniform voltage depression. Those concepts have been developed further and applied to the DEMO gyrotron design in 2016.

The coaxial insert, fixed at the MIG of the gyrotron and reaching through the cavity area, is intended to rarefy the mode spectrum in the cavity, and consequently, reduce mode competition and increase operation stability. In order to achieve this, it is tapered and has longitudinal corrugations in the cavity. While the typical dimensions within the cavity are of the order of 1 mm (free-space wavelength at 238 GHz: 1.26 mm; required corrugation width/depth: ca. 0.3 mm), the insert length is around 50 cm, leading to a maximum permitted tilt of below 0.1°. As gyrotrons are welded and evacuated after assembly, misalignment compensation can only be achieved using the magnetic field (electron beam position) or external screws (insert position/tilt), which might be possible only up to a certain precision. Therefore, investigation on effects of residual misalignments of electron beam and coaxial insert is important.

Effect of insert misalignment on the TE modes

For insert misalignment below 1 mm, the deformed main mode as well as its competitors remain practically constant with the cavity wall, as has been demonstrated using the 2D eigenmodes solver of COMSOL. Correspondingly, mode eigenvalues (i.e. eigenfrequencies) and couplings to the electron beam do not change significantly. However, those small changes can influence the outcome of time-dependent multi-mode interaction simulations substantially, which is why the properties of the deformed modes have to be determined with high precision. In view of this, the code SCNCHIMP has been developed, which can express the Transverse Electric (TE) modes of a misaligned cavity in terms of TE modes in rotationally symmetric cavities. SCNCHIMP is developed to address

- Misalignment up to 1 mm,
- Eigenvalues up to 180,
- Eigenvalue precision of 10^{-7} , and
- Azimuthal indices m up to 60.

The corrugated insert is described using the surface impedance model (SIM), provided the corrugation width is sufficiently smaller than the azimuthal wavelength. The underlying calculations are based on a field decomposition over axial cross-sections that has been adapted from the literature to determine mode eigenvalues more efficiently, supplemented by routines that ensure consistent mode numbering along the cavity axis. An interface from SCNCHIMP to the code-package EURIDICE for gyrotron interaction simulations has been initiated and needs further verification until reliable interaction simulation results can be obtained.

Besides the stray radiation in the gyrotron due to parasitic modes generated by beam-wave interaction or by a non-perfect quasi-optical mode converter (launcher) and mirrors, there is additional stray radiation because of the coaxial insert. This stray radiation is caused by the inevitable mode conversion at the end of the insert and it increases rapidly with increasing insert misalignment. Increased levels of stray radiation can impede proper operation of the tube. Using the above mentioned field decomposition one can determine the ratio of powers between stray radiation and proper radiation. More details are given in Fig. 1.5.3.

For the coaxial-cavity design considered here, an insert misalignment above 150 μm would lead to an in-gyrotron stray radiation of 4 % (additionally to the other sources of stray radiation). This level would probably be too high for reliable operation at 2 MW.

Effect of insert misalignment on the electron beam

Since typical modes remain concentric with the cavity wall, as long as the coaxial insert is only moderately misaligned (which covers all reasonable scenarios), the electron beam has to be kept aligned with the cavity wall as well, in order to couple well to the operating mode. Unfortunately, such a configuration leads to

inhomogeneous electrostatic potential (voltage depression) around the beam circumference, and, consequently to an increase of the kinetic energy spread of the beam electrons and therefore a reduction of the interaction efficiency. In order to quantify this reduction a detailed description of the voltage depression distribution is necessary.

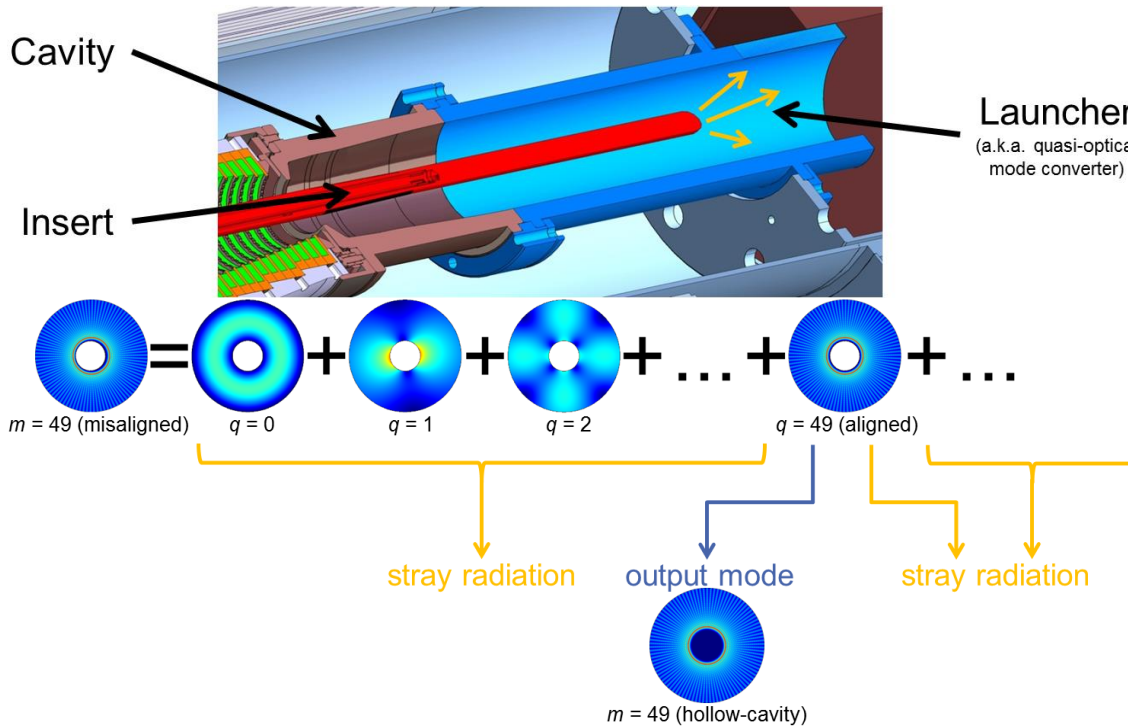


Fig. 1.5.3: Upper: Cavity, insert and launcher of a coaxial-cavity gyrotron. The origin of insert-induced stray radiation is indicated by orange arrows. Lower: Schematic field decomposition of the misaligned-cavity mode $TE_{49,29}$ into aligned-cavity field components q , and subsequent extraction of hollow-cavity mode $TE_{49,29}$ from the dominant field component $q=m=49$. Field components of azimuthal symmetries other than $q=49$, as well as (mostly) the Neumann part of component $q=49$ will contribute to stray radiation after the end of the coaxial insert, leaving only the Bessel part of component $q=49$ as the desired hollow-cavity mode $TE_{49,29}$ with the design frequency.

In practically no geometry, except for perfect alignment, voltage depression can be expressed in closed analytic form. However, using truncated series of mirror charges, it was shown that it is possible to find excellent approximations for the voltage depression on beam electrons in arbitrarily misaligned cavities (including hollow cavities) and with arbitrary beam shapes. In the coaxial-cavity design considered here, a misalignment of $500 \mu\text{m}$ leads to an energy variation of 1 keV (1.17 % of the beam kinetic energy), which would probably impede proper gyrotron operation severely. Therefore, the aforementioned maximum misalignment of $150 \mu\text{m}$ seems to be a reasonable value also if voltage depression is considered.

Hollow-cavity 1 MW design

For DEMO ECRH&CD, the fundamental design of a 236 GHz, 1 MW hollow-cavity gyrotron has been initiated in 2014. Considering the multi-frequency operation of the gyrotron for multi-purpose operations, suitable operating modes have been chosen at 170 GHz, 203 GHz, 236 GHz and 269 GHz. Using a systematic cavity design approach, all the physical parameters of the interaction section have been fixed and the optimum operating parameters of gyrotron have been finalised, taking into account the interaction efficiency requirement and a wall loading limit of 2 kW/cm^2 . The feasibility of the design is further verified for a 2-3 GHz fast-frequency step-tunability, to achieve plasma instability control with a fixed EC launcher. The beam misalignment tolerance has also been estimated using a new macro-electron beam based technique.

The realistic electron beam parameters (velocity spread: 6 % (rms), radial width: $\lambda/4$) and realistic conductivity of Glidcop material have been used for the multi-mode, time-dependent simulations, which suggest stable output of 920 kW with an interaction efficiency of 36 % (without depressed collector). As per the EUROfusion baseline 2012, in total 50 MW power are required for ECRH&CD application. High output power per tube is always desirable, which eventually leads to a minimised number of tubes per plant, as this will increase reliability and cost-effectiveness of the heating system.

In 2016, different generic approaches were suggested to identify the mode eigenvalue limit for stable operation considering mode competition. This limit is directly related to the power limit for the hollow cavity concept. After obtaining the eigenvalue limit, a new cavity design and operating parameters are proposed for 1.5 MW, 236 GHz gyrotron operation. The possibilities of an advanced, triode start-up scenario were also investigated.

Eigenvalue Limit Analysis

The solution for high power operation is to use a very high order mode (e.g. eigenvalue > 103 for a 236 GHz gyrotron). For a particular hollow-cavity operating mode, its eigenvalue is a root of the derivative of the Bessel function. As the radius of a cavity is directly proportional to the mode eigenvalue, by using a high-order mode it is possible to increase the area of the cavity wall, which significantly reduces the maximum wall-loading. However, it should be noted that the mode spectrum density increases with high order modes and it may not be possible to excite the desired mode, due to critically high mode competition. For a particular operating frequency, it is very important to know the eigenvalue limits for stable operation, which would allow choosing the most suitable mode within the eigenvalue limit and thus achieve the highest output power.

The list of selected modes for this analysis is presented in Table 1.5.2. Within an eigenvalue range from 105 to 145, nine modes are selected with approximate eigenvalue separation of 5 and having a relative caustic radius of 0.41. The selected modes are named as 'DM1' to 'DM9' in ascending order of eigenvalue. Different cavity geometries are considered for analysis, in which the radius of the interaction section is selected according to the operating modes. The cavity radius increases with the eigenvalue, which increase the total power handling capability of the cavity for the same wall-loading. Due to the same relative caustic radius, the behavior of these modes is identical, except the mode competition: mode competition increases linearly with the increase in eigenvalue.

To investigate the effects of mode competition, two generic approaches are suggested using linear and non-linear gyrotron theory. Considering the linear, fixed-field theory of the gyrotron, the influence of the electron beam on the field profile is neglected and the mode eigenvalue limit is estimated using (i) starting current calculations and (ii) analysis of the mode coupling versus frequency. These methods suggest a stable gyrotron operation until a mode eigenvalue of 125 (DM5 mode), which corresponds to the output power of 1.5 MW.

Table 1.5.2: Selected high-order modes considered for this analysis with their corresponding parameters. All the selected modes are having nearly same relative caustic radius of 0.41-0.42.

Mode name	DM0	DM1	DM2	DM3	DM4	DM5	DM6	DM7	DM8	DM9
Mode	TE _{43,15}	TE _{44,15}	TE _{45,16}	TE _{48,17}	TE _{50,17}	TE _{52,18}	TE _{53,19}	TE _{56,20}	TE _{58,20}	TE _{59,21}
Eigenvalue	103.21	104.46	109.17	116.4	118.91	124.87	129.58	136.8	139.32	144.02
Cavity radius (mm)	20.88	21.14	22.09	23.55	24.06	25.26	26.22	27.68	28.19	29.14
Beam radius (mm)	9.06	9.28	9.49	10.10	10.51	10.93	11.13	11.75	12.16	12.37
Rel.caustic radius	0.41	0.42	0.41	0.41	0.42	0.42	0.41	0.41	0.42	0.41
Diffractive Q	1443	1445	1457	1483	1493	1573	1533	1553	1559	1567

In the case of non-linear, self-consistent theory, the modification of the axial field profile due to the high-frequency component of the electron beam is taken into account. Initially, the optimized operating parameters for the individual operating mode are determined considering only single-mode interaction without including the neighbouring modes in the self-consistent interaction simulations with EURIDICE. In the single-mode case, the stable operation is achieved with all selected modes (DM1-DM9). As a next step, all the neighbouring modes being within the -5 % to +10 % frequency range and having a relative coupling coefficient of more than 50% are selected for the multi-mode, time-dependent, self-consistent simulations of the diode start-up. In Fig. 1.5.4, the RF behaviour of the DM5 mode (eigenvalue ~ 125) and DM7 (eigenvalue ~ 135) are compared. In the case of DM5, the stable excitation of the operating mode TE_{52,18} is possible. On the other hand, because of the dense mode spectrum, the desired operating mode TE_{56,20} is not excited in the case of DM7. This analysis of the selected modes using non-linear, self-consistent, multi-mode simulations also suggests mode eigenvalue limit of 125 for a 236 GHz hollow-cavity gyrotron.

In summary, assuming diode start-up and realistic electron beam parameters, both suggested methods predict stable operation with modes having eigenvalues up to 125, which corresponds to a maximum output power of around 1.5 MW.

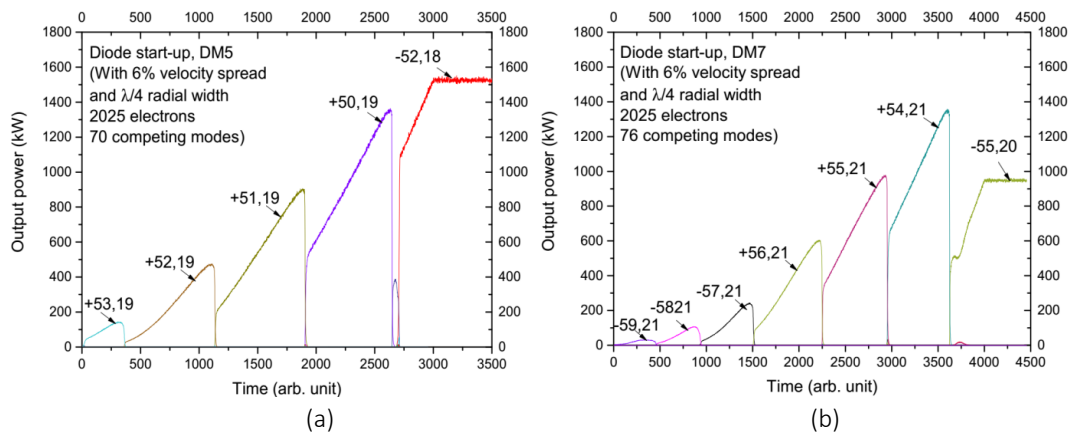


Fig. 1.5.4: Multi-mode, self-consistent, diode start-up analysis for (a) DM5 and (b) DM7 mode.

Triode type start-up scenario

The triode-type start-up scenario has been investigated to control mode competition with high-order modes, which can further increase the output power. In Fig. 1.5.5 the diode-type start-up scenario is compared with the triode-type start-up scenario: In diode start-up, the beam energy increases linearly with the applied accelerating voltage, while the velocity ratio α is increasing following the adiabatic approximation. In the case of triode start-up, using the modulation anode, the velocity ratio can be controlled individually. The triode start-up scenario was proven to be an effective method to control mode competition and stable output could be achieved until a mode eigenvalue of 145 (DM9). The modes excited during the start-up process can be controlled by a proper selection of the transition phase, i.e. of the voltage range in which the velocity ratio is quickly increased.

In the case of a hollow cavity gyrotron, the voltage depression is very critical for high-order volume modes. The detailed analysis of the effects of space charge neutralisation is under investigation. In addition to that, the possibilities of new hybrid-type start-up scenarios should be also studied, which consider neutralisation effects during a slow triode start-up.

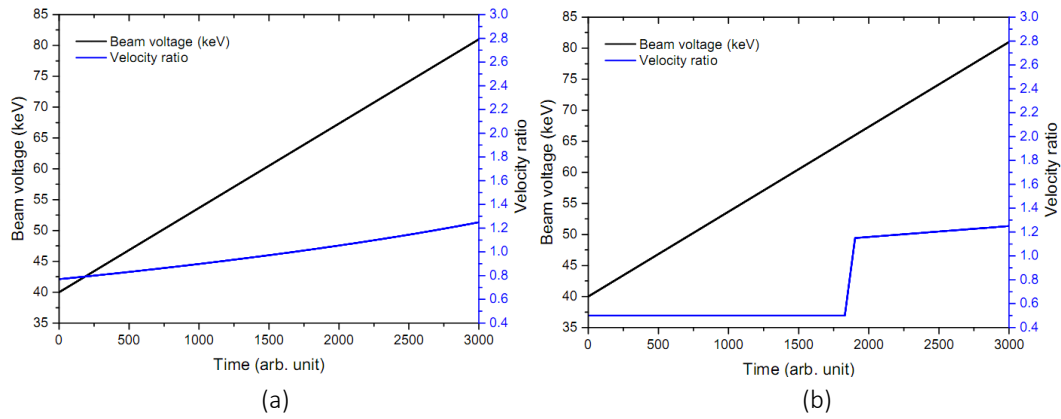


Fig. 1.5.5: Comparison of (a) diode type and (b) triode-type start-up scenarios.

1.5.3 Upgrade of the code-package EURIDICE to address coupled modes

An upgrade of the code-package EURIDICE for gyrotron interaction simulations and cavity design has been initiated, in order to simulate the interaction of an electron beam with azimuthally coupled electromagnetic modes in gyrotron cavities that are not rotationally symmetric. The motivation has been the support of studies, within EUROfusion PPPT WPHCD, involving such cavities. These are coaxial cavities with mode-converting corrugations on the outer wall (Z. C. Ioannidis et al., *Journal of Infrared, Millimeter, and Terahertz Waves* 36, 2015) and coaxial cavities with misaligned coaxial insert (see section 1.5.2). The upgrade has been completed in terms of mathematical formulation and programming. Work on creating interfaces between EURIDICE and the codes calculating the electromagnetic field structure in coaxial cavities with corrugated outer wall or misaligned insert has also been initiated.

Representation of the high-frequency electromagnetic field

In the gyrotron cavity, the electron beam is assumed to excite TE modes. The high-frequency electromagnetic field at the vicinity of the electron beam is represented as a sum of TE modes of a cylindrical (or coaxial) waveguide. All field components of a TE mode can be derived from its axial magnetic field $\text{Re}\{H_z\}$, where:

$$H_z = f(z)\psi(r, \varphi, z)e^{i\omega t}.$$

The eigenfunction ψ describes the transverse structure of the electromagnetic field and the field profile function $f(z)$ describes the axial structure along the cavity axis z . The eigenfunction ψ may slightly vary along z -axis, to account for the mild axial non-uniformity of the geometry. It obeys the Helmholtz equation at each cross section:

$$\nabla_{\perp}^2 \psi(r, \varphi; z) + k_{\perp}^2(z) \psi(r, \varphi; z) = 0, \quad k_{\perp} = \chi / R_o,$$

where χ is the mode eigenvalue, obtained from the characteristic equation involving the boundary conditions for the field in the transverse cross section, and R_o is the radius of the cavity's outer wall.

The average stored electromagnetic energy can be calculated as

$$W_{em} \approx 2W_e = \frac{1}{2} \int_{z_{in}}^{z_{out}} \frac{Z_0}{c} \left[\frac{\omega^2}{c^2 k_{\perp}^2} \right] \frac{|f(z)|^2}{k_{\perp}^2 C^2} dz, \quad Z_0 = (\mu_0 / \varepsilon_0)^{1/2}, \quad C^2 \triangleq \frac{1}{\iint_{S(z)} |\nabla_{\perp} \psi|^2 dS},$$

where $S(z)$ is the surface of the resonator cross-section at position z . The average ohmic wall loading of the outer (o) and inner (i) wall at each cross section can be written as:

$$\rho_{o,i}(z) = Z_0 \frac{\pi \delta}{2 \lambda} \left[C_{zo,i}(z) |f(z)|^2 + C_{\perp o,i}(z) \frac{1}{k_{\perp}^2} |f'(z)|^2 \right],$$

where $\lambda = 2\pi c / \omega$ and the unitless positive quantities $C_{zo,i}$, $C_{\perp o,i}$ can be evaluated using the expressions for the electromagnetic field.

EURIDICE upgrade

For rotationally symmetric gyrotron cavities, the eigenfunction $\psi_{mp}(r, \varphi; z)$ of a TE_{mp} mode at the vicinity of the electron beam has the form:

$$\psi_{mp}(r, \varphi; z) = \left[A J_m(k_{\perp mp} r) + B Y_m(k_{\perp mp} r) \right] e^{-im\varphi}, \quad k_{\perp mp} = \frac{\chi_{mp}(z)}{R_o(z)}, \quad (1.5.1)$$

where the integer m is the azimuthal index of the mode, and J and Y are the Bessel and Neumann function, respectively. In the case of the hollow cylindrical cavity, $A = 1$, $B = 0$, and the eigenvalue χ_{mp} is the p -th root of the characteristic equation $J_m'(\chi) = 0$. In the case of a coaxial cavity with smooth insert or with an insert with impedance corrugation, we have $A = 1$, $B = -J_m'(\chi_{mp}) / Y_m'(\chi_{mp})$, and the eigenvalue χ_{mp} is the p -th root of the characteristic equation (9) in (Iatrou et al., IEEE Trans. Microwave Theory Tech. 44, 1996).

All these rotationally symmetric cases can be addressed by EURIDICE, that is, the eigenvalue χ_{mp} , the eigenfunction ψ_{mp} , and the relevant coefficients C^2 , $C_{zo,i}$, $C_{\perp o,i}$ are calculated and are used for the simulation of the beam-wave interaction. However, in the case of non-rotationally symmetric cases, the eigenfunction has the following expression, which reflects the coupling of azimuthal modes invoked by the breaking of the rotational symmetry:

$$\psi_{mp}(r, \varphi; z) = \sum_{q=1}^N \left[A_q J_{m+n_q}(k_{\perp mp} r) + B_q Y_{m+n_q}(k_{\perp mp} r) \right] e^{-i(m+n_q)\varphi}, \quad k_{\perp mp} = \frac{\chi_{mp}}{R_o}. \quad (1.5.2)$$

Here, n_q is integer and the sum over q is limited to N terms (rather than infinite terms) for numerical reasons, assuming that N is chosen as large as necessary for the field to be described with the appropriate

accuracy. The expression 1.5.1) is consistent both with that for coaxial cavities with mode-converting corrugations on the outer wall, and with that for coaxial cavities with misaligned corrugated insert.

The calculation of the eigenfunctions of the resonant modes in the non-symmetric cases, i.e. the calculation of the eigenvalues χ_{mp} and the coefficients A_q, B_q , is a complex task and dedicated codes have been developed, namely CCCI (Z. C. Ioannidis et al., *Journal of Infrared, Millimeter, and Terahertz Waves* 36, 2015) for the coaxial cavities with corrugations on the outer wall, and SCNCHIMP (see section 1.4.2) for the coaxial cavities with misaligned insert. Since the eigenfunctions and the coefficients $C^2, C_{z0,i}, C_{\perp0,i}$ are necessary for beam-wave interaction simulations in EURIDICE, an interface file has been designed, which will be used to import these quantities from CCCI and SCNCHIMP to EURIDICE. The usage of the interface file has been implemented in EURIDICE.

The generalisation of the eigenfunction expression from (1.5.1) to (1.5.2) has additional consequences besides the change in the coefficients $C^2, C_{z0,i}, C_{\perp0,i}$. It also affects the coupling coefficient G_{mp} between the electron beam and the TE_{mp} mode. The expression for G_{mp} in the rotationally symmetric case is the following:

$$G_{mp} = AJ_{m-s}(k_{\perp mp} r_{gc}) + BY_{m-s}(k_{\perp mp} r_{gc}),$$

where r_{gc} is the radius of the guiding centre of the electron on the transverse plane and s is the cyclotron harmonic number. After the generalisation (1.5.2) for the eigenfunction, the expression for the beam coupling coefficient has to be updated accordingly. This was done and the new expression was numerically implemented in EURIDICE, both in the interaction codes and in the code for the calculation of the starting currents of the modes.

1.5.4 Specifications for a superconducting magnet and contacts with suppliers

The objective has been the detailing of the specifications of a 10.5 T superconducting magnet (SCM), to support the > 200 GHz gyrotron development towards DEMO. Contact to magnet suppliers has been already initiated, kept up, and intensified during the years 2014 and 2015. At the beginning of 2016, it was decided to send requests for a tentative budgetary offer to possible suppliers. For this request, a list of requirements, which has been already defined in the year 2015 has been slightly relaxed to increase chances to get reasonable budgetary offers from possible suppliers. The maximum on-axis magnetic induction at the center of the cavity will be 10,5 T, the minimum borehole diameter will be 240 mm. In order to ensure a high flexibility the different coils must be controlled individually.

In March 2016, a number of possible suppliers have been contacted and asked for budgetary offers based on the relaxed list of requirements. This started intensive discussions during the following months (via e-mail, video-conferences and direct visits of company representatives at KIT), indicating critical challenging problems of the proposed requirements. After July 2016, two additional companies were contacted and they also showed interest in this project.

The response received from several companies during 2016 finally indicated that the construction of the proposed 10.5 T magnet is feasible. Based on the gained information, a detailed list of specifications started to be compiled at the end of 2016, in order to launch a call for tender in the first quarter of 2017.

1.5.5 Investigations on multistage depressed collectors

The study of Multistage Depressed Collectors (MDC) has been continued. In particular, more studies on the collectors based on $E \times B$ drift have been done. The conceptual idea proposed in the previous year has been

studied in details. A systematic way has been found to optimise the auxiliary coils in the MDC to transform the annular electron beam to sheet beams. With this method, the thickness of the sheet beam can be optimised. Since the thickness of the sheet electron beam is related to the efficiency of the $\mathbf{E} \times \mathbf{B}$ MDC, the understanding of the way to optimise the magnetic field for the beam-shape transformation is important. Moreover, three new ideas on concepts for $\mathbf{E} \times \mathbf{B}$ collectors, intended to be simpler than the concept proposed in the previous year, have been investigated. Conceptual models have been simulated, yielding promising results. The first two concepts are based on the $B_z \times E_y$ drift. In the first concept, the annular electron beam is transformed to an elongated elliptic beam. The elongated elliptic electron beam can be handled like a sheet beam and a known technique for sheet electron beams (Pagonakis et al., *Physics of Plasmas* 23, 2016) can be directly used to collect this elliptic electron beam. The second concept splits the annular electron beam to two sheet beams in semi-circle shapes. It is based on the same principle as the first concept, but can handle the annular electron beams, which enclose high magnetic flux. The third concept is based on $B_z \times E_\phi$ drift. The azimuthal component of electric field is created by a pair of helical electrodes and the drift is radial in this case.

Optimization of the magnetic field for the previous MDC concept

In the previous “wing” concept, the coils used to transform the electron beam should only have current in axial direction. The coils have arc-shape cross sections, shown in Fig. 1.5.6. This may not be the optimum shape. In order to describe the magnetic field lines in a better way, the flux coordinate (a.k.a. Clebsch form of magnetic field) is used. The magnetic flux density \mathbf{B} in Clebsch form is formulated by the cross product of two scalars:

$$\mathbf{B} = \nabla\alpha \times \nabla\beta .$$

In this special case, all relevant coil currents are axial, i.e., $\mathbf{J} = \hat{\mathbf{z}}J_z$. After decomposing the 3D system into transversal (α) and axial (β) components, the field lines in a transversal cross section can be represented only with the parameter α :

$$\nabla^2\alpha = J_z \tag{1.5.3}$$

The value for the magnetic field line indicator α in (1.5.3) can be obtained with Green’s function. With this mathematical tool, the thickness of the transformed electron beam can be optimised. This optimisation results in an electron beam much thinner than before, as compared in Fig. 1.5.6 (blue curves denote the optimised beam). Since a thinner electron beam yields higher collector efficiency, for this specific design a simulation with 5 stages shows 86 – 88 % collector efficiency. The secondary electrons and reflected electrons are totally recaptured inside the collector; no electron returns to the mirror box. A collector efficiency of 82 % can thus be achieved even in the presence of secondary electrons.

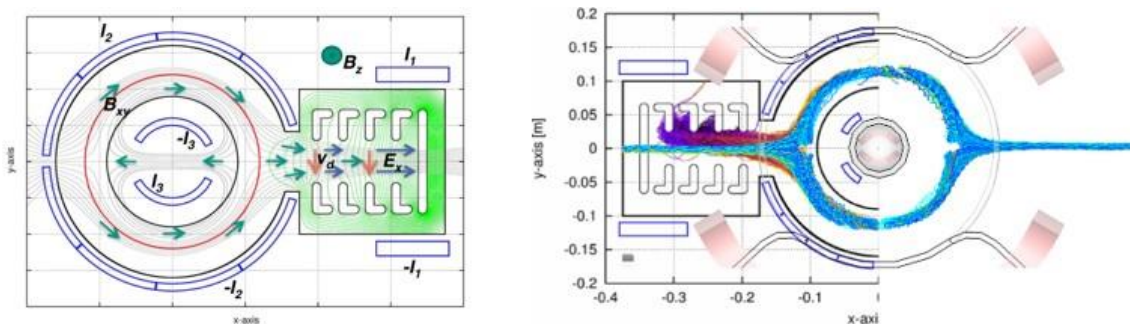


Fig. 1.5.6: Left: The previous $\mathbf{E} \times \mathbf{B}$ concept. Right: Beam thickness before and after optimizations.

Concept with an elongated elliptic electron beam

Another idea to obtain a thin electron beam is to use transversal currents, which refocus the small-orbit annular beam to a thin elliptic beam. The transform is done by four transversal currents, presented in Fig. 1.5.7 as the long edges of each coil. The injected electron beam travels towards the positive z-direction. The long edges of the left hand side coil defocus the electron beam only in y-direction, whereas the next coil on the right hand side refocuses the beam in x-direction. Additionally, ferromagnetic slices can be placed in the coil loops to reduce their current requirement.

Under the condition that no electron will return back to the mirror box the minimal length of the collector i.e., the minimal axial length of the electrodes can be calculated through

$$L > L_{\min} = \frac{2 \Psi q}{\pi m_0 \min\{v_0\}} \quad (1.5.4)$$

where Ψ is the magnetic flux (converged value) enclosed in the electron beam and v_0 are the initial velocities of the electrons.

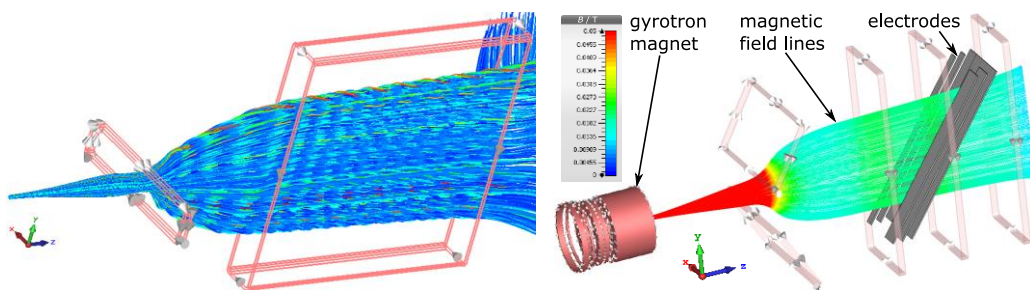


Fig. 1.5.7: Transformation of elliptic beam.

Concept with semi-circle electron beams

An additional idea to obtain thin sheet beams is to sacrifice a small fraction of the electrons. In this way, the hollow electron beam is split into two semi-circular beams, which then can be collected on several pairs of electrodes, where each pair of electrodes has the same depression voltage. Moreover, the shape of electrodes may not be straight like in the previous section. Instead, the edges are adapted to the profile of the electron beams, as shown in Fig. 1.5.8. The required length for this kind of MDC can also be analytically calculated in the way similar to (1.5.4). Splitting the electron beam does not only decrease the MDC length (compared to the full elliptic beam variant), but also improves efficiency, since the split beams are just as thin as the thickness of the cyclotron motion. The efficiency improvement gained from the wafer-thin beam overcomes the energy lost in the sacrificed electrons. A specific simulation of a three-stage collector based on this concept has 76.5 % efficiency, considering secondary electrons and the effects of space charge.

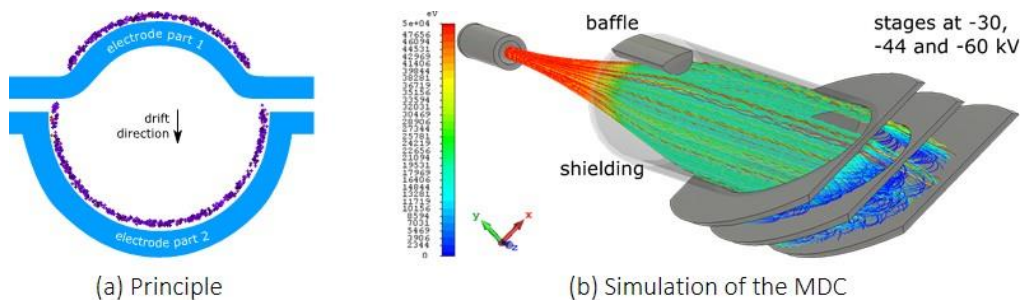


Fig. 1.5.8: Split a circular electron beam to semi-circular sheet beams.

Concept using helical electrodes

Another new concept, which utilises an azimuthal electric field and the longitudinal magnetic field has been considered. This concept does not transform the electron beam to sheet beams, therefore, it has a simpler geometry. It is based on a normal conic single-stage collector. The novel point here is that a helical slot splits the collector into two stages and induces an azimuthal (φ) component of electric field, illustrated in Fig. 1.5.9. The torsion of the helix defines the angle between the electric and magnetic field, and thus it is related to the strength of the $\mathbf{E} \times \mathbf{B}$ drift.

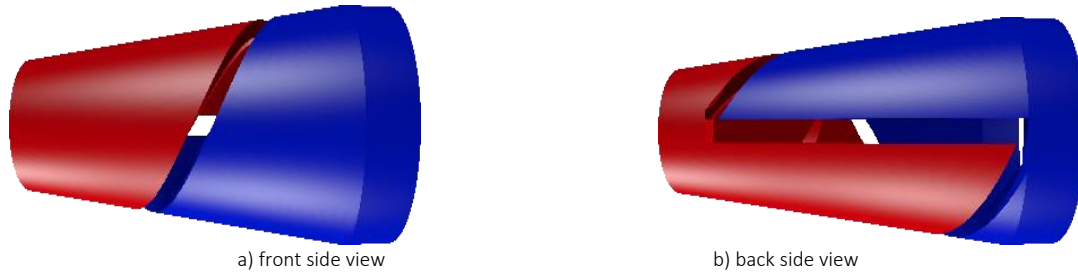


Fig. 1.5.9: Two stages separated by a conical helix slot for the $\mathbf{E} \times \mathbf{B}$ drift.

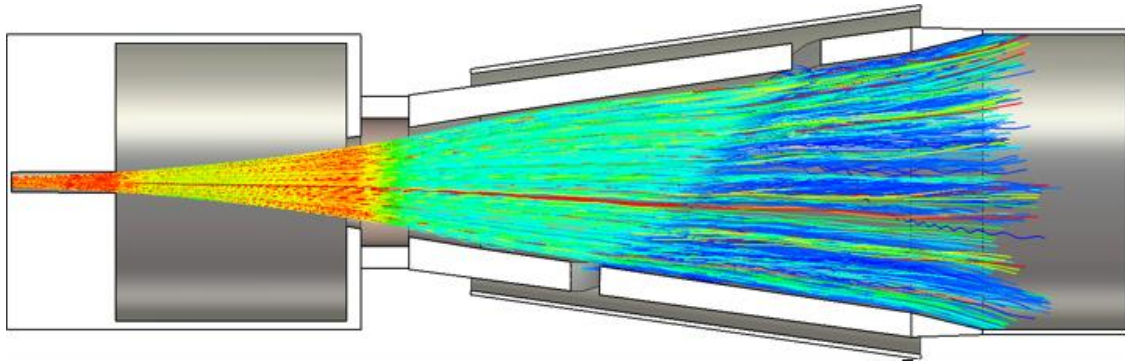


Fig. 1.5.10: Simulation of a two-stage collector with helical slot.

A special model is simulated, as shown in Fig. 1.5.10. This two-stage collector works like the other $\mathbf{E} \times \mathbf{B}$ MDCs in such a way that the low-energetic electrons are drifting to the helical slot and impact the first electrode with -30 kV depression, whereas the high-energetic electrons are drifting to the second electrode with -42 kV depression. Taking secondary electrons into account, PIC simulations with CST Particle Studio show an average collector efficiency η_{col} of 77 % (compare to the state-of-the-art single-stage depressed collector $\eta_{\text{col}} < 60$ %). Secondary electrons only reduce the efficiency by 1 %. There could be less than 1.5 % of the total beam current returned beyond the mirror box (including secondary electrons). The returned current can be reduced by controlling the width of the straight slot connecting both helix ends, which can be further optimised.

1.5.6 Studies towards a 140 GHz 1.5 MW CW gyrotron for W7-X

A preliminary investigation on a possible upgrade of the 140 GHz 1 MW CW gyrotron for W7-X has been performed, with the target to increase the power of the ECRH system of the stellarator. The focus of the research has been on more than one design branches, in order to determine the feasibility of designing a tube with the specified technical goals, while maintaining flexibility with respect to the specific technical realisation. The work focused on mode selection and on preliminary design of the gyrotron cavity and launcher.

To find suitable operating modes for operation at 140 GHz, 1.5 MW, the candidate modes were divided into two categories according to their performance with respect to the ohmic wall loading. In the first category, modes exhibiting ohmic wall loading of the same level as that in the existing 1 MW gyrotron for W7-X ($\sim 1.5 \text{ kW/cm}^2$) were considered. This is a conservative approach, based on the experimentally successful performance of the series CW tubes for W7-X. In the second category, modes with ohmic wall loading of the level of that in the EU CW gyrotron for ITER ($\sim 2 \text{ kW/cm}^2$) were considered. This is a realistic approach, provided that the performance of the cavity cooling of the ITER gyrotron will be experimentally verified in CW operation. In both categories, the possibility of efficient dual-frequency operation with a second frequency at 175 GHz was also taken into account. After the selection of the best mode out of each category, two cavities were designed and optimised for the respective modes. Finally, for each of these two cavities a quasi-optical launcher was also designed. The best candidate mode from the first category was proven to be the $\text{TE}_{28,13}$ mode and the best candidate from the second category was the $\text{TE}_{32,9}$ mode. Their simulated performance is summarised in Table 1.5.3.

Table 1.5.3: Operating modes for operation at 140 GHz, 1.5 MW CW.

Modes @ 140 GHz	$\text{TE}_{28,13}$	$\text{TE}_{32,9}$
Beam voltage	80 kV	80 kV
Beam current	51 A	51 A
Magnetic field	5.57 T	5.57 T
Output power at the cavity	1.69 MW	1.69 MW
Ohmic wall loading	1.56 kW/cm^2	2.14 kW/cm^2
Interaction efficiency	43%	43%
Frequency	140.42 GHz	140.40 GHz

Following this investigation, an additional search for suitable modes was conducted, now with the goal of achieving an upgrade of the existing W7-X gyrotron with a minimum of design changes. The target was set to 1.3-1.5 MW and the requirement for highly efficient dual-frequency operation was relaxed. In order to keep the same electron gun as in the W7-X gyrotron operating in the $\text{TE}_{28,8}$ mode, the beam radius was kept the same, which confined the candidate modes to the $m = 28$ mode series. The candidate modes are given in Table 1.5.4, along with the simulated performance assuming a beam voltage of 80 kV and a typical cavity length of 8 free-space wave lengths. The best choice is the $\text{TE}_{28,10}$ mode, which can achieve 1.5 MW and has an eigenvalue which is lower than the one of the $\text{TE}_{32,9}$ mode, already successfully excited in the EU gyrotron for ITER. In addition, the $\text{TE}_{28,10}$ mode requires a cavity radius which is only 2.3 mm larger than the one of the existing cavity of the $\text{TE}_{28,8}$ W7-X gyrotron. Such a small increase can be easily accommodated within the existing cavity design, inducing only minor changes in the cooling structure.

Table 1.5.4: Operating modes in the $m = 28$ mode-series.

Mode	TE _{28,9}	TE _{28,10}	TE _{28,11}	TE _{28,12}	TE _{28,13}
Eigenvalue	63.6261	67.1036	70.5435	73.9521	77.3344
Cavity radius	21.64 mm	22.82 mm	23.99 mm	25.15 mm	26.3 mm
Beam radius	10.01 mm				
Beam current	48 A	54 A	60 A	67 A	74 A
Output power at cavity	1.45 MW	1.65 MW	1.83 MW	2.17 MW	2.41 MW
Ohmic wall loading	2.10 kW/cm ²	2.07 kW/cm ²	2.06 kW/cm ²	2.08 kW/cm ²	2.07 kW/cm ²

1.5.7 Studies towards an 60 GHz, 1 MW CW gyrotron for Collective Thomson Scattering applications in ITER

The Collective Thomson Scattering (CTS) diagnostic is crucial for understanding the dynamics of ions in the plasma. From considerations of spatial resolution, plasma access, scattering cross section and current or potential availability of sources, only a few frequencies are relevant. The only CTS system which can meet the ITER measurement requirements is a 60 GHz system. Most demanding for this system is the development of a 1 MW gyrotron at 60 GHz. Additionally to the specifications regarding the frequency and output power, another requirement, related to the spectrum of the electromagnetic wave, is very important: The power in spurious modes within the ± 5 GHz range around the central frequency of 60 GHz must be more than 100 dB lower compared to the power at 60 GHz.

A preliminary study on the feasibility of an 60 GHz, 1 MW CW gyrotron for CTS in ITER was performed. Two gyrotron cavity designs were obtained. The operating mode of the first design is the TE_{18,6} mode. Following standard mode-selection procedures that take into account the physical and technical limitations and target at maximisation of the efficiency, this mode was proven to be the best candidate. However, with a required cavity radius of 32.4 mm and an electron beam radius of 15.2 mm, such a gyrotron would be larger than all KIT-related gyrotrons and thus the development of a completely new gyrotron would be necessary for the realisation of the design. The second design was based on the dimensions of the existing 140 GHz gyrotron for the stellarator W7-X to facilitate a possible manufacturing. The operating mode of the second design is the TE_{12,4} mode. With a cavity radius of 20.9 mm and a beam radius of 10.2 mm, the dimensions are close to the radial dimensions of the W7-X gyrotron.

Both cavities were optimised by a parameter study with respect to the cavity length. The cavity length was finally set to 8λ for the TE_{18,6} design and to 7λ for the TE_{12,4} design, where $\lambda = 5$ mm is the free-space wavelength at 60 GHz. In multimode simulations, both designs were found capable of producing 1.1 MW of output power at an operating frequency of 60 GHz without any competing modes excited. The calculated performance is summarised in Table 1.5.5.

Finally, the spectrum of the generated microwave radiation was investigated to check if the gyrotrons meet the challenging CTS requirements regarding the purity of the spectrum. The level of purity of the spectrum was found stable with respect to the operating voltage. The spurious power components in the ± 5 GHz range around the central frequency were down to ~ 95 dB lower than the central spectral line in the simulations. This is in agreement with the high spectral purity required by CTS.

Table 1.5.5: Calculated performance of the two cavity designs.

Operating mode	TE _{18,6}	TE _{12,4}
Operating frequency	60.069 GHz	60.055 GHz
Output power at cavity	1.097 MW	1.092 MW
Peak ohmic wall loading	0.478 kW/cm ²	0.928 kW/cm ²
Interaction efficiency	43.1 %	42.1 %
Normalised field amplitude, F	0.159	0.208
Normalised interaction length, μ	12.870	11.499
Normalised detuning parameter, Δ	0.574	0.645

1.6 FULGOR (Fusion Long-Pulse Gyrotron Laboratory)

The existing gyrotron test facility at KIT, which had been designed and built about 30 years ago, plays a worldwide leading role in the development of high-power gyrotrons for nuclear fusion applications. This facility offered the unique opportunity to develop and test the first CW high power series gyrotrons for the stellarator W7-X in collaboration with IPP and Thales Electron Devices as the industrial partner.

The target parameters of the new gyrotron test facility are well beyond the capabilities of the existing one. The new test stand will strongly support KIT's leading role in the development of advanced gyrotrons. It will help to answer the questions regarding the technical limits and new physical designs for future high-power microwave tubes. The key parameters of FULGOR will be:

- Full CW operation with up to 10 MW electrical power
(corresponding to ≥ 4 MW RF power (assuming an efficiency of the gyrotron ≥ 40 %)
- Support of advanced energy recovery concepts, e.g. multi-stage depressed collector (MSDC)

The high voltage power supply (HVPS) will support an operating voltage of up to 130 kV with up to 120 A beam current in short pulse operation and 90 kV / 120 A in continuous wave regime. A superconducting magnet which allows operation of gyrotrons at frequencies well above 200 GHz will be a major component of FULGOR. Other significant components of the teststand will be: cooling system, control electronics and interlock system, RF diagnostics including high-power RF absorber loads.

The capabilities of FULGOR will enable the development and CW tests of gyrotrons for future fusion machines like ITER and DEMO. Fig. 1.6.1 is a simplified CAD view of the complete FULGOR system.



Fig. 1.6.1: CAD view of FULGOR installation including control room.

Substantial progress has been achieved in the planning, procurement and installation of major systems of the new test stand.

High Voltage Power Supply (HV PS): In 2016 the final design details of the HV PS have been discussed and agreed with the supplier (Ampegon, Switzerland (CH)). The production of components has been started and the installation of major elements has been performed (see Fig. 1.6.2 and Fig. 1.6.3). The production of the sub-assemblies of the EPSM power modules (84 in total) for CW operation has been started and first electrical and mechanical tests show a proper behavior. The procurement of components and the production of the Pulsed Power System modules (PPS modules) (40 in total) for up to 5 ms operation have been started.



Fig. 1.6.2: Left: Two 6.5 MVA transformer installed at FULGOR hall. Right: Ventilation cabin and rack for electronic modules.

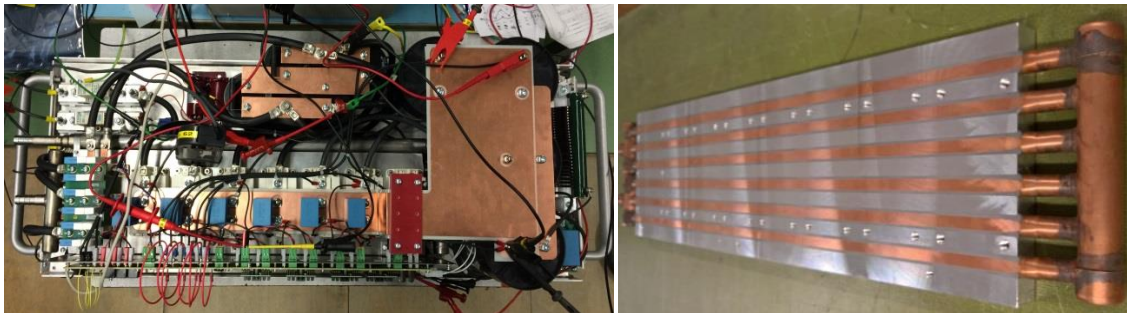


Fig. 1.6.3: Power module and cooling unit.

Cooling system: The cooling system is designed for full 10 MW operation. However, in the first step only a first single tower with a cooling power of 5 MW was installed (see Fig. 1.8.4), with the option to add a similar second tower at a later stage for full 10 MW CW cooling capacity. All pumps, piping, instrumentation and control has been installed, partially tested and accepted.

Control and data acquisition: The strategy for control of the HVPS has been discussed and decided with the supplier (Ampegon). Several components of industrial standard Siemens S7 have been procured and implemented. First components of a fast interlock system to limit the energy deposition in the tube in case of malfunction, fast data acquisition to record events occurring on a μs timescale and visualisation have been implemented and tested.

Superconducting magnet: This is the most challenging component of the FULGOR project since the requirements are far beyond what is the today's industrial standard. In particular, a large borehole diameter (min. 240 mm (target: 270 mm)) in combination with a high magnetic field requirement (up to 10.5 T to ensure gyrotron operation up to 240 GHz) calls for a very clever design of the magnet. In 2016 intense discussions with several industrial supplier took place in order to clarify technical solutions and to come to realistic specifications.



Fig. 1.6.4. 5 MW cooling tower (left) and cooling pipes in FULGOR hall (right).

Involved Staff:

KIT/IHM: K. Avramidis, J. Franck, M. Fuchs, **Dr. G. Gantenbein**, **Dr. S. Illy**, Dr. Z. Ioannidis, Prof. J. Jelonek, Dr. J. Jin, Th. Kobarg, R. Lang, W. Leonhardt, M. Losert, D. Mellein, A. Meier (KIT, IAM-AWP), Dr. I. Pagonakis, A. Papenfuß, K. Parth, S. Ruess (KIT CS), **Dr. T. Rzesnicki**, Prof. Dr. Theo A. Scherer (KIT, IAM-AWP), M. Schmid, W. Spiess, Dr. D. Strauss (KIT, IAW-AWP), Prof. M. Thumm, S. Wadle, J. Weggen, Ch. Wu, A. Zein, J. Zhang, **IGVP (University of Stuttgart):** **Dr. W. Kasperek**, Dr. C. Lechte, R. Munk, Dr. B. Plaum, F. Remppel, H. Röhlinger, B. Roth, K.H. Schlüter, S. Wolf, A. Zeitler, **IPP (Greifswald/Garching):** B. Berndt, Dr. H. Braune, F. Hollmann, L. Jonitz, **Dr. H. Laqua**, Dr. S. Marsen, F. Noke, M. Preynas, F. Purps, A. Reintrog, T. Schulz, T. Stange, P. Uhren, M. Weißgerber, F. Wilde